Advances in Environmental Technology 10(3) 2024, 237-269.

Iranian Reasearch Organization for Science and Technology (IROST)

Advances in Environmental Technology

Journal home page: https://aet.irost.ir

CFD with the Population Balance Model for Packed Bed Airlift Reactor with External Loop

Shivanand Teli[a], Sunil Kulkarni*[b]

[a] *Three D Engineering Automation LLP, Pune, Maharashtra.*

[b] *Chemical Engineering Department, Gharda Institute Technology, Lavel, India.*

ARTICLE INFO

Document Type:
Research Paper

Article history:
Received 21 February 2024
Received in revised form
1 May 2024
Accepted 9 May 2024

Keywords:
Computational Fluid Dynamics, External Loop Airlift Reactor, Fixed Bed, Population Balance Model, Shear Sensitivity

ABSTRACT

An airlift reactor with the external loop (EXL ALFR) is a widely used modified version of a Bubble Column Reactor (BCR). An EXL ALFR can also be used for a three-phase system with the solid phase in a packed or fluidized form. An EXL ALFR provides design flexibility for conventional chemical reactions as well as biological reactions. Shear is an important factor for the reactors handling immobilized enzymes. In the current investigation, the effect of the design variables, like gas hold-up, the velocity of circulating liquid, and the distribution of bubble dimension, was compared for an EXL ALFR and an external loop airlift reactor with a packed bed (EXL ALFR-PB). Particle Image Velocimetry (PIV) was employed for the liquid axial velocity in the downcomer of the reactors, and the computational fluid dynamic with the Population Balance Model (CFD-PBM) was employed. The minimum percentage of errors of 2.3% and 1.2% and the maximum of 4.2% and 3.4% were obtained for the experimental and predicted values of gas hold-up in the EXL ALFR and EXL ALFR-PB, respectively. For the velocity of the circulating liquid, the predicted and experimental values of their minimum percentage error were 1.1% and 0.5% and a maximum of 4.3% and 4.5% in EXL ALFR and EXL ALFR-PB, respectively. Also, the pressure drops calculated from the Ergun equation and CFD simulation had a 0 to 4% difference, indicating good agreement.

1. Introduction

The biological treatment processes can be aerobic and anaerobic. In anaerobic reactors, the organic matter decomposes in the absence of oxygen or air to form methane and other gases. The anaerobic methodology is preferred for heavy slu with high oxygen demand. Different contactors for anaerobic treatment can be used: anaerobic lagoons, sludge blanket reactors (anaerobic up flow, expanded and baffles flow), and anaerobic filter reactors. Aerobic reactors include stirred tanks, bubble columns, fluidized beds, and airlift reactors. Aeration is a very important aspect of the reactors used in aerobic treatment. In aerobic treatments of wastewater, the important parameters that need to be monitored are the economy and efficiency in terms of pollutant

*Corresponding author Tel.: +91 96 64213953
E-mail: suniljayantkulkarni@gmail.com
DOI: 10.22104/AET.2024.6677.1824

removal and energy consumption, cost, and discharge quality.

Modern-day research for treating wastewater is driven by the need to recycle wastewater, making it reusable and recyclable. Bubble column reactors, airlift reactors, fluidized bed reactors, and stirred tank reactors are being investigated by the experts to model and optimize them for maximum efficiency and economy. The position of the impellers, aeration ports, baffles, and stirrers, as well as the size of the bubbles formed, flowrate, and properties of biological sludge, are the most investigated parameters for optimization and modeling. In the airlift loop, the gas is flown through a compartment to mobilize and circulate the broth or flocs between outer compartment and inner compartment. Low power consumption, effective dispersion, simplicity, and low contamination are advantages of airlift reactors. Energy demand, foaming, and possible cell damage are drawbacks of these contactors. Investigations on airlift reactors focus on optimizing the operating parameters and reducing the limitations.

Biological three-phase systems, such as fermenters, bioreactors, or wastewater treatment plants, use contacting equipment such as stirred tanks, bubble columns, three-phase fluidized columns, and airlift reactors. Operating problems in these contact equipment include adversities in keeping up steadiness and the slow rate of the bioprocess in a bioreactor due to inadequate mixing [1]. Insufficient mixing may be due to poor construction and design [2, 3]. Mixing in the bioreactors is required for the uniformity of the pH, to maintain the tight contact of various components, and to prevent fouling, foaming, and thermal stratification. The ALFR for gas liquid contacting has a wide range of applications in the industry. ALFRs are classified into two categories based on circulation loops, namely external and internal loop reactors [4, 5]. The excellent mixing and prolonged contact time for gas-liquid flow are facilitated in ALFR. The reverse mixing in the liquid phase and elevated values pressure drop are the two main limitations of a bubble column reactor. Modification minimizes these limitations in an airlift reactor with an external loop. Thus, an EXL ALFR can be considered a customized reactor with the principles of a bubble contactor. The velocity in the riser section of an EXL ALFR is invariably higher than in the bubble column contactor.

Gas-liquid-solid fluidized beds (GLS-FBD) are considered very efficient devices for three-phase operations. Many researchers have reported investigations on the hydrodynamics of gas-solid-liquid (GLS) flow in a FBD [6–10]. A FBD contactor is a highly complex mixture of GLS flow in the reactor. The effect of the jetting, the formation of bubbles in the fluid, the movement of the suspended particles, and pressure variations increase the stochasticity in the characterization of the bed [11]. The external loop airlift bioreactor can be superior to the FBD. The most important advantage of EXL ALFR lies in controlling the velocity of the circulating liquid in a reactor. A well-directed pattern can be achieved in EXL ALFR, resulting in reduced shear stress, which is crucial for cultivating shear-sensitive organisms. Due to this advantage, ALFR is widely used in biochemical processes [12]. Gas-liquid contactors are widely used for biological reactions involving fermentation and enzyme catalysis. Turbulent stresses during synthesis, upstream processing of enzymes, and enzyme activities cause the change in enzyme structures that results in loss of enzyme activity [13]. EXL ALFR facilitates well-defined flow patterns, resulting in a reduction in a considerable amount of shear stress that is crucial for the cultivation of shear-sensitive organisms [12]. The estimation of different hydrodynamic parameters during gas-solid–liquid flow in an airlift reactor is one of the major outcomes of past works [14–20]. EXL ALFR finds application in GLS systems containing solids in downcomer sections. Flexibility in manipulating GLS mass transfer and maximum shear are advantages of such systems. An airlift fluidized bed reactor can manipulate the design parameters by optimizing the riser to downcomer ratio and superficial gas velocity reported in earlier work [21].

Knowledge about hydrodynamics in the airlift reactor with external loop with a fixed/packed bed is the key to equipment design and process optimization. The velocity of circulating liquid is a critical design factor for airlift reactors [22]. It governs the design parameters, namely effective interfacial area for gas-liquid contact, mass

transfer rate, degree of liquid-phase mixing, and heat transfer rate at the wall. The gas hold-up (ϵ) determines the residence time of the bubble in the liquid phase. The gas-liquid interfacial area, the efficiency of gas-liquid mass transfer, and the velocity of circulating liquid in ALFR are governed by the liquid hold-up. There is a strong relation between the maximum value of the gas hold-up that needs to be accommodated and the total design volume, and hence the bioreactor design parameters [23]. The coexistence of single-phase (downcomer) and multiphase makes EXL ALFR-PB hydrodynamics a little complicated; hence, treating it as a solitary reactor is a challenging task [24].

In EXL ALFR, homogeneous and heterogeneous flow regimes are reported in the literature [25, 26]. The uniformed sphere-shaped bubbles are formed at a homogenous flow regime at low superficial gas velocity. The bubble merging and its breaking in the reactors become more intense, and the size distribution of the bubble varies with a superficial gas velocity. It indicates that the flow pattern has altered from a similar phase region to a dissimilar phase regime [27]. Therefore, it is envisaged that the bubble coalescence and break-up be considered for realistic hydrodynamic predictions. The CFD-PBM (computational fluid dynamics-population balance model) can be employed to alter the prediction accuracy for the betterment of accurately predicting the hydrodynamics of the external loop airlift reactors. In the past, many researchers have used it with considerable success [27–30]. A literature survey indicates that work on a CFD-PBM study in an EXL ALFR with a fixed bed is a rarity.

The current investigation studied the effect of the gas flow parameters on the various factors related to the mass transfer and bubble size distribution (BSD) of the EXL ALFR and EXL ALFR-PB, which were quantified and compared. The PIV technique provided a detailed characterization of the local and overall hydrodynamics of an EXL ALFR and EXL ALFR-PB. A three-dimensional approach was employed to simulate the airlift contactor for the reactor. The commercial CFD package ANSYS CFX 14, which utilizes the finite element method to solve the discretized system of equations representing the flow, was used. Furthermore, the incorporated CFD-PBM with bubble coalescing and break-up models was employed. In the PBM, the bubble coalescence and break-up models were very important for realistic predictions of the hydrodynamic parameters in an airlift reactor with external loop with a fixed bed. The coupling of the PBM into a CFD framework enabled a better understanding of the hydrodynamic behavior of a gas-liquid flow in a reactor.

1.1. Literature review on multiphase contactors for wastewater treatment

Multiphase contactors are required in wastewater treatment, especially biological wastewater treatment methods. The effluent from industry or households contains various impurities. These contaminants can be putrescible and nonputrescible. The former can be biodegraded, and the latter cannot. Aerobic and anaerobic methods of wastewater treatment have different byproducts. The aerobic bacteria are used to stabilize organic matter in the aerobic pathway. In unsaturated sludge, demanding oxygen is used by microorganisms and converted into settleable sludge. Carbon dioxide and water are generally products of aerobic treatment. Different types of contactors are used for wastewater treatment by using aerobic methods. The activated sludge process, biological contactors, stirred tanks, packed/trickle beds, and fluidized beds can be used for wastewater treatment. The fluidized beds and packed beds have different applications in aerobic and anaerobic wastewater treatments. In the activated sludge process, air or oxygen is bubbled from the bottom. Also, sparged vessels, circulating packed beds, and stirred tank reactors can be used for the treatment. The efficiency of the treatment in biological processes is a strong function of the sludge age and sludge concentration. In the case of a stirred tank, its function is affected by the position of the impellers, baffles, and pore size of the gas inlets. The size of the packing, recirculation rate (if any), flowrate, and effluent concentrations are important factors of a packed bed. The bubble size has recently been identified as a very important factor in the contactor. In addition to these, trickle bed contactors can also be used. The biological slime plays a very important role in these trickle beds or biotowers. The reactor or contactor used in the treatment process depends on the

nature of the wastewater and its content. Agricultural wastewater contains nutrients. The degradation of these nutrients is a very important aspect of this treatment. Sevugamoorthy and Rangarajan employed phycoremediation for agricultural wastewater [31]. They carried out their investigation with three types of algae. They found suitable species for the treatment. The other methods associated with wastewater treatment are membrane separation, advanced oxidation, photobiological treatment, and different advanced treatments, including cavitations and chemical treatments.

Kus and Madejski used CFD modeling to study the multiphase flow for a two-phase condenser ejector system [32]. The local structure of multiphase flow for various parameters could be studied using CFD. Complex phenomena influencing the flow could be analyzed. They used a Splading/evaporation model for the direct contact condensation of steam [32]. The applicability and reliability of multiphase CFD studies improved because of sensitivity studies [33]. Near wall mesh size has a significant effect on the multiphase CFD model results for condensation. Yang et al. developed a robust CFD model in their investigation [33].

Conventional wastewater treatment methods are being modified for better efficiency and cost-effectiveness. In the current scenario of industrialization and ever-increasing population, the reuse of wastewater is becoming a necessary aspect of the treatment. The removal of pathogens is very important for making water reusable. The degradation of phenol by a novel method was reported by Majhool et al. [34]. In an ozonized bubble column reactor, they used zinc oxide nanoparticles. A combination of various treatment techniques is being explored for the removal of novel contaminants. Nanotechnology plays a very important role in these treatments. The antipathogenic properties of silver nanoparticles can be utilized for such wastewater treatment [35]. Combining biological principles with nanotechnology can handle tricky and emerging contaminants in wastewater [36]. To minimize the process energy requirements, investigations are focused on finding optimum operational conditions [37]. El Aissaoui El Meliani et al. analyzed the activated sludge-based process for such optimization [37].

Multiphase fluid bed reactors were used for the Fenton treatment of wastewater by Sharma et al. [38]. They discussed improvement in the Fenton process by the application of a fluidized bed. According to them, fluidization positively impacted the Fenton process for wastewater treatment. One major drawback of the Fenton process is the formation of a large amount of sludge. The fluidized reactor can be utilized in combination with the Fenton process to solve this problem. An investigation on a foam block type of stirring system in a reactor used for textile wastewater treatment was carried out by Yang et al. [39]. In ozone treatment, this type of stirrer increased the mass transfer coefficient. For this purpose, the stirrer facilitated the customization of gas hydrodynamics and operating conditions. They prepared synthetic, simulated textile wastewater with Acid Red B. This investigation provided the fundamentals for a foam stirred tank reactor for wastewater treatment. Kandasamya and Venkatachalam studied a multiphase reactor with the help of three components [40]. They used waster and different concentrations of glycerol along with monoethylene amine (Newtonian), carboxy methyl cellulose9non (Newtonian), and different types of particles. They investigated the voidage effect on various parameters, like size, shape, flowrate, and other viscosity-related properties.

Hydrodynamic and kinetics studies have been reported on the bubble and stirred aerated processes [41,42]. Bubble fluidizations help reduce temperature gradients and, in view of the strong exothermic nature of the oxidation, help the treatment process. The aerobic sludge can be used to remove nutrients from wastewater. Effective granulation and removal of nutrients were attempted by Desireddy and Sabumon [43]. The contactor used was a sequential batch airlift reactor that facilitated the effective removal of nutrients without alkaline conditions and very little sludge formation. The wastewater from the spent oil and the water produced from that wastewater had a high level of hydrocarbon toxicity. Due to this, the removal of these materials was essential before disposing of the wastewater. Bacterial lipids

could be produced from this wastewater in airlift reactors. Silva et al. used two reactors in sequence for the treatment of the produced water effluent and lubricant based effluent [44]. Thus, sequential batch reactors could be used for the valorization of wastewater contaminants.

1.2. Past work on CFD applications for mutiphase reactors in wastewater treatment

The equipment used for wastewater treatment can be continuous stirred tank reactors (CSTR), packed reactors, bubble reactors, trickle beds, etc. CSTR is one of the commonly investigated and used contactor in wastewater treatment. CSTR has excellent characteristics with respect to mixing, stability of the system, and adaptability. Pravin Kumar et al. used a numerical method for designing a CSTR [45]. They used a multiphase CSTR model in their work. They utilized the Navier Stokes model (Reynold average) for the turbulence. They considered water as the primary liquid phase and the sludge as the secondary phase. In their work, they developed the Eulerian model with the application of CFD and the approach of particle distribution. In the proximity of the tank wall, they observed that it was possible to enhance the dispersion of the sludge and the reliability with adaptive refinement of the mesh. The effluent, microorganisms and their interrelation played an important role in the mass transfer. Also, the density of the sludge and rheological properties played an important role in the wastewater treatment. The high value of viscosity and sludge density affected the performance. Basically, the high sludge density led to the formation of inactive zones. In this work, the distribution of the sludge was predicted using Ansys fluent software. In their investigation, Pravin Kumar et al. held major phase (liquid) properties constant and only altered the secondary properties [45]. A more pronounced distribution of sludge could be obtained by using thick sludge, but it needed more energy.

CFD was used with the multiphase volume method for studying the wastewater treatment accompanying cavitation by Sekar et al. [46]. Their investigation focused on the formation, growth, and effect of cavitation. CFD tools were applied for simulating and analyzing the characteristics of the reactor with respect to its performance. CFD, thus, played a very important role in the reactor design and optimization. Understanding the characteristics and the interplay between various affecting parameters with the quality factors enabled the optimization of the treatment process. Breaking the pollutant structure was an important aspect of the treatment. This could be achieved by using the strategy of changing the length of the throats, thereby increasing removal efficiency. In this investigation, the numerical method enabled the estimation of the effect of the divergent angle in the formation of liquid to water vapor. The results related to the breakup of the bubble and coalescence could be better analyzed by using the discrete particle model methodology. Cavitation led to a very effective degradation of dyes. The CSTR is suitable for the treatment of wastewater. The cavitation reactor is also a very effective option for removing pollutants from wastewater. Parameter optimization has made it possible to save energy. Parameter optimization by applying CFD is a boon for scientists in the simulation and optimization of the conditions for wastewater treatment. Thus, wastewater treatment is also being modernized to remove pollutants and make water reusable by using modern simulation methods encompassing various tools like CFD and Ansys Fluent.

Hydrodynamic effects were compared for the airlift reactor by Ni et al. [47]. Diffused aeration was employed in most of the aerators, resulting in the energy cost accounting for about 45% to 75%. Optimizing this energy with diffuser positions and other parameters led to an energy-efficient operation. In their investigation, Ni et al. used single and multi-bubble size models [47]. They employed CFD with a PBM model to study the effects of various parameters on the cavitation of hydrodynamic type, namely the diameter of the bubble, the distribution of inlet gas, and the rate of flow of fluid. According to these studies, the multiple bubble distribution type of model was able to fit the data. The model results agreed with the experiment's results with 5% accuracy. The sensitivities of the distribution of the bubble size varied according to the flowrates. The identicalness between the coefficient of lift and the critical diameter was underlined in the simulation studies. The application of the multiple bubble model effectively predicted the tower system

characteristics. The lesser size of the inlet bubble and the high velocity of the gas increased the column circulation and, hence, intensified the same. At high gas velocities, it was seen that the bubble size distribution was not sensitive enough.

Elaissaoui Elmeliani et al. investigated the ozonation contactor for disinfecting wastewater [48]. For rendering disinfective status to the wastewater, the inactivation of the coliform is a very important aspect. These are gram-negative and non-motile bacteria that are non-spore forming and are capable of the synthesis of acid and gases. They used 3D CFD simulation to study and optimize the parameters for an ozone contactor. The parameters considered for increasing effectiveness were the flowrate and ozone concentration. Even distribution of ozone was important, along with improving the mass transfer efficiency. The introduction of new injection points and design optimization was carried out to enhance the ozone distribution and mass transfer. They employed the Chick-Watson model for predicting the disinfection kinetics. More than 99% and close to 100% disinfection was achieved after optimization. Thus, the problem of poor mass transfer and uneven distribution of ozone was effectively solved. The CFD tool also played a very important role in this optimization. Picking the proper model for the reactor system plays a crucial role in the success of the modeling. Simulation of the reactor system and its modeling aspects provide a cost-effective and time- efficient solution for the treatment of wastewater. This investigation by Elaissaoui Elmeliani underlined the role simulation and CFD play in modern wastewater treatment facilities [48].

The reactions that are difficult thermodynamically can be facilitated by using plasma catalysis. Plasma technology is used with CFD application to carry out reactions and convert the effluent components into another compound. The CFD tool plays a very vital role in designing and optimizing plasma reactors [49]. Various complexities in turbulence, multiphase flow, and transport processes are unraveled by using CFD. Various industrial processes can be reshaped with the application of plasma hybrid modeling. The sophisticated and efficient computational techniques and machine learning methods empower scientists to intensify reaction systems. Comfort et al. used the mixing model approach [50]. The CFD results were converted into material balance equations for the components. They generated the compartment model and coupled it into the Monod type model for biokinetics. They exported the CFD data into a table that contained cell centered data. In this work, geometric bounds were determined using the X, Y, and Z minimum and maximum values. In this work, the compartment models were prepared for two tank geometries. These models were used to perform the dynamic mixing simulations. From the data obtained from the compartment and CFD model results, it was concluded that these two models showed similar results and agreed with each other. According to this investigation, there was a need to handle grid resolution with the utmost care as it could have a significant effect on the results. By coupling the simple compartment model with the biokinetic model, a fermentation (240 minutes) was successfully simulated. The concentration gradient and its effect on the overall process was successfully analyzed. The method developed in this investigation could handle the results of CFD from different software, mesh, and geometry. Hydrolysis phenomenon and water distribution in anaerobic biological treatment could be optimized using simulation tools [51]. In treating persistent contaminants, the treatment was hindered by dead zones and short circuits. The interactions between the solid and liquid phases could be made uniform, and water distribution could be improved by using CFD simulations. Also, for improving the treatment efficiency, hydrolysis acidification could be utilized. They obtained a chemical oxygen demand reduction of 15% to 29% and color removal of 50% using this treatment method.

Cold plasma activation aided by microbubble was used successfully for wastewater treatment by Gao et al. [52]. Cold plasma discharges are capable of successfully degrading a variety of contaminants. Microbubbles were formed using the cavitation technique and incorporating an active plasma discharge species. Sulfathiazole was a sample contaminant targeted for removal. For activation efficiency, the width of the cavitation tube was detected as an important and most crucial parameter. According to the results obtained in

this investigation, a wider inlet could result in a greater number of bubbles and increased air volume fraction. The degradation percentage obtained by linear multiple regression and the artificial neural network were in very good agreement.

In wastewater treatment, aeration is used to stabilize organic matter. The aerators used in the tanks should be capable of diffusing the air properly. Investigations are reported on the different layout patterns for aerators and their effect on the air distribution and quality of mixing in the tank [53]. In many cases, the aerators have shown poor performance due to various factors, including diffusor positioning. Interactions and mixing of the bubbles and the involved liquid-gas systems play a vital role in the mass transfer. These two factors were factored for five diffuser systems using CFD by SeyedSharifi et al. [53]. They used an Ansys design modeling pre-processor to show the geometry of the model. They observed that in the lateral pattern, there was the development of spiral flow from the outer to the inner wall. Also, due to the placement of diffusers in a transverse fashion and the lack of axial flow producer propellers, a similar rotational bulk flow could not form throughout the tank. The pattern of the grid confirmed the existence of a complex mixing pattern. It was also observed that there was axial flow completely in the area that was not aerated. They assigned weights to three of the most important criteria: quality of mixing, size of bubbles, and distribution of air. In this weightage system, 0.2 weightage was given to air distribution, the bubble size was given the highest weightage of 0.5, and mixing quality was 0.3. According to this study, the lateral, checkered, and line patterns maintained the velocity well above 0.3 m/s, whereas other patterns, namely stripe and grid patterns, dissipated the energy of the flow. The lateral, checkered, and line patterns could be used for maximum efficiency. The research also indicated that these patterns could effectively be used for more complicated systems involving biological reactions and chemical reaction-related models. The flow fields and the associated phenomenon could be studied with more accuracy with the proposed patterns. These positive results could enable fast and effective decision-making regarding the flow parameters and diffuser patterns for various applications.

In their investigation for modeling an electrocoagulation reactor for fluoride removal from the wastewater, Jin et al. proposed the use of three models, namely CFD, growth mechanism, and light transfer models [54]. The CFD model enabled the simulation of a gas-liquid flow multiphase system and the tracking of the particles, mainly microalgae. The photobioreactor light intensity was tracked using the light transfer model. With the help of the light intensity and position of the particles, the local growth rate was calculated, and then the integration of these local rates yielded the total growth rate. The results of the experiments carried out with a flat plate photobioreactor and stirred bioreactor were compared with those obtained from the integrated model. It was found that the results were in good agreement. The consistency in the simulation data and the experimental results and their close agreement with each other indicated that the integrated model was capable of describing the kinetics of microalgae under large scale conditions. The integrated model was a good alternative to the dynamic growth model in the transient photobioreactor. The stirring rate was an important factor; a low stirring rate might result in the settling of microalgae, and a very high one in a waste of energy. Also, the resulting high shear may harm the microalgae.

Teli and Kulkarni used two configurations of impellers in their investigation for better wastewater treatment [55]. They found the degradation of pollutants was less at low superficial velocities. According to the study, the impeller speed and gas velocity directly affected the gas hold-up, and hence largely affected the mass transfer coefficients. They obtained a maximum degradation of 80% at the impeller speed of 170 revolutions per minute (rpm).

Traditional wastewater treatment systems involving biomass face the challenge of the uniform distribution of air, biomass, and other quality parameters for waste degradation. CFD estimation of the performance of the reactor is very important for improving the quality of the treatment methodology. A novel approach using a double partition stirred vessel was adopted by

Zhang et al. in their investigation [56]. The impellers in this research were located in an eccentric fashion. The sample wastewater used for the treatment was wastewater from biomass ethanol production. The RNG turbulent k-epsilon model was used to simulate the flow of fluid. In order to maintain the concentration in the vicinity of the blade, they ensured the circulation of the fluid by designing a special type of weir crest and pores that were used for interconnection. Their investigation revealed that the pattern of flow in the tank was independent of the Reynolds number. Sadino-Riquelme et al. classified strategies to integrate kinetic modeling and fluid dynamics [57]. According to their study, a kinetics coupled CFD application had a cost disadvantage. The computational cost was too high in this case, and it was necessary to simplify the model to reduce it, which could result in inferior results. Another approach is CFD uncoupled kinetics, which is a cost-effective and easy approach but inadequate for real-time simulations. The latter strategy is used if the models are based on the compartmental approach. This leads to indirect coupling of the CFD to the kinetics. This strategy is a practical solution for a cost-effective approach for real time simulation.

Hernández-Rodríguez investigated the effect of biogas bubbles on the hydrodynamics in the upflow anaerobic sludge flow reactor (UASB) for wastewater treatment [58]. In this investigation, a solar heater was used for temperature control. The plug flow pattern was predominant in the reactor. However, after consideration of the bubble distribution, the plug flow pattern changed into a completely mixed flow pattern. Sutudehnezhad et al. carried out studies on the effect of the design of aerators on the fouling, mixing, and scouring ability of a membrane in a flat sheet membrane bioreactor [59]. To improve the economy and efficiency, they proposed angular nozzles. They used response surface methodology-based design of experiments for finding the optimum nozzle diameter and a CFD tool for simulations. This angular nozzle exhibited a higher wall shear and better removal of fouling. Also, the nozzle made a higher volume fraction of the air possible.

In wastewater treatment, a large amount of sludge is produced. The disposal of this sludge may pose a solid waste problem. Burning this sludge and utilizing the combustion enthalpy can have twin benefits of sludge reduction and heat utilization. An investigation was carried out by Dottei et al. on the combustion of sewage sludge in a fluidized bed reactor [60]. They employed the Eulerian approach and a formulated thermal model in their work related to simulation. They carried out a methodological comparison of the results in 2D and 3D studies. According to them, a 3D approach was more expensive and could be used based on the objective of the study. If a quantitative evaluation of the flow is required for the entire contactor, then it is advisable to use the 3D approach. The mixing behavior of the sludge and the fluidization-related behavior can be studied using 2D models. 2D simulation can be considered as a suitable method for simulations in the case of a preliminary investigation.

The primary objective of the work is to establish the ability of an airlift reactor with an external loop as a gas-liquid-solid contactor without direct contact of the solids with the gas phase. The bubble coalescence and break-up models are employed in the present simulation. The hydrodynamic parameters for EXL ALFR-PB and EXL ALFR are compared for the same operating condition. The CFD model of an airlift reactor with an external loop with and without a fixed bed is used to establish the system's behavior by analyzing the effect of different design variables and the system's response to the changes in operating parameters. A CFD model is evolved for designing and scaling-up an airlift reactor with an external loop with a fixed bed for immobilized enzymes that may be sensitive to shear and direct contact with the gaseous phase.

2. Materials and methods

The experimental work was done in an airlift reactor with an external loop of acrylic pipes. The diameter of the riser section was 0.094 m, and that of the downcomer was 0.039 m. Both were connected at the top by a crown with a 0.240 m diameter called a disengagement zone. A baffle plate of 0.1 m height was placed vertically, separating the crown into two parts. The liquid from the riser flowed down past this baffle, allowing the air bubbles to leave from the top

instead of getting entrained into the downcomer section. Both the pipes were joined together at the bottom by an elbow. A gas sparger with five openings was placed at the bottom of the riser just above the height where the downcomer met the riser. A fixed bed of spherical balls was fixed in the downcomer section, supported by a mesh. The diameter of the steel ball was 0.00435m, and the height of the packed area was 0.10m. The sphericity of packing material was 0.87. The voidage of packing was 0.67. The diameter of each of the five-hole openings in the sparger was 0.0015 m.

Air was forced through the 0.0015m openings of the sparger by a compressor. Five different gas flowrates in EXL ALFR and EXL ALFR with a fixed bed reactor were used. The corresponding superficial gas velocities were 0.02 m/s, 0.04 m/s, 0.06 m/s, 0.08, and 0.10 m/s. A pressure transducer and conductivity probes were used to measure the hold-up of the gas and circulation velocity of the liquid. The top and bottom riser sections were connected with probes for pressure and conductivity measurement (Fig.1). The liquid axial velocities in the downcomer section at (H = 400 mm) are measured using PIV (PIV) (Fig. 2). The axial velocity profiles of the liquid were determined in EXL ALFR and EXL ALFR with a fixed bed reactor for different superficial gas velocities and compared with CFD simulation results. The schematic diagram of the airlift reactor with an external loop with a fixed bed is shown in Fig. 1. Fig. 2 depicts PIV in an airlift reactor with external loop with a fixed bed.

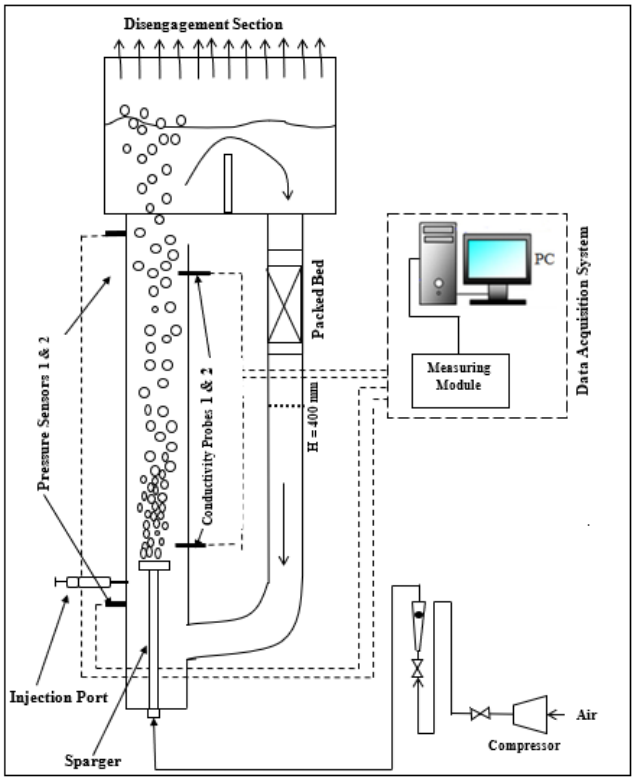

Fig. 1. Schematic diagram of airlift reactor with external loop with a fixed bed.

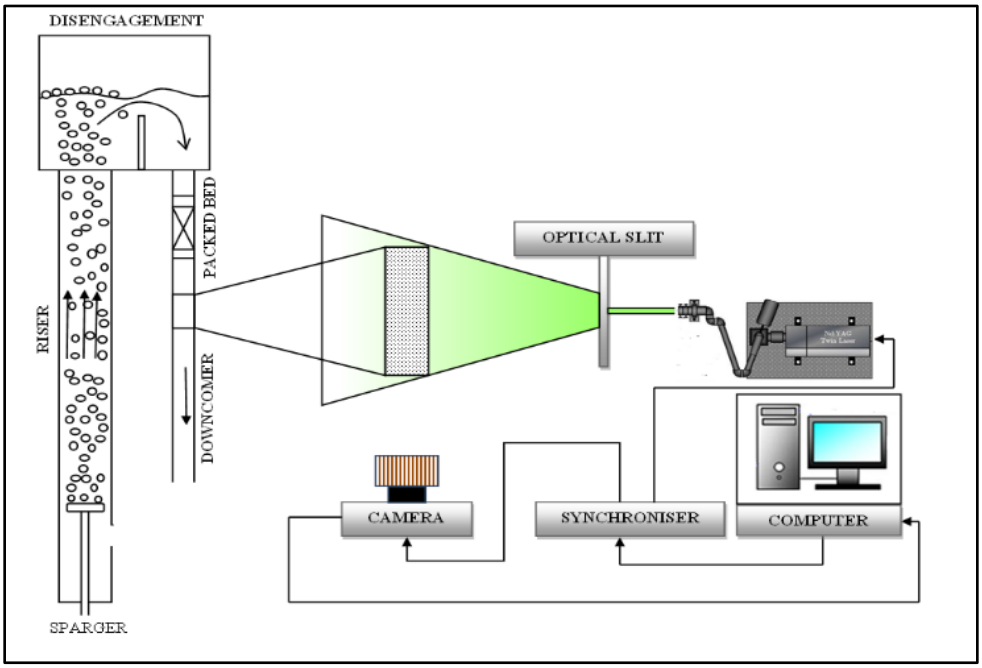

Fig. 2. Schematic diagram of PIV in an airlift reactor with external loop with a fixed bed.

3. Parameters Estimated

An experimental investigation was carried out to study the effect of various parameters related to hydrodynamics that have an effect on the mass transfer. The gas volume inside the reactor, along with the velocity of the fluids, had a significant effect on the performance.

3.1 Gas hold-up (ϵ_G)

The gas hold-up is obtained using the condition of homogenous and heterogeneous flow regimes; for heterogeneous flow regimes, the liquid exhibits higher turbulence levels. In such a case, an average pressure fluctuation value is considered for each operating condition. The gas hold-up in the riser was obtained using the following equation reported in the literature [61]:

$$\epsilon_G = \left[1 - \frac{\Delta P}{\Delta P_O}\right] \quad (1)$$

where ΔP is the dynamic pressure drop at $U_G > 0$, measured by a pressure sensor located in the riser section, as shown in Fig. 1. ΔP_O is the measured liquid hydrostatic head at $U_G = 0$. The pressure drop was determined by the pressure sensors placed in the riser at a 1 m distance and adjusted to 0-30 psi. The pressure data sampling frequency was 60 H_Z.

3.2. Velocity of circulating liquid (U_L)

The riser section's liquid linear velocity (v_r) was estimated using a tracer dose method [62, 63]. Two conductivity probes were employed for monitoring the conductivity. Two probes were at 3 from each other and placed in plastic tubing. They were joined to the computer via an interface circuit (Fig. 1). The conductivity meter at 10 Hz frequency was used and consisted of an analogy-to-digital/digital-to-analogy converter (ADC/DAC). The conductivity ranges of 0 to 2.0 mS and 0 to 20 mS were used. The conductivity probes had a maximum response time of one second. 2 ml potassium chloride solution was forced into the riser as a pulse input. The liquid linear velocity was affected by the distance between the probes and the time gap between the conductivity peaks. The liquid linear velocity in the riser was determined by Eq. 2.

$$v_r = \frac{d_e}{t_p} \quad (2)$$

where d_e is the vertical distance between the probes and t_p is the time interval between the conductivity peaks.

The velocity of circulating liquid in the riser (U_{Lr}) was determined from Eq. 3.

$$U_{Lr} = (1 - \epsilon_G)v_r \quad (3)$$

Similarly, the velocity of circulating liquid in the downcomer was measured using the continuity equation.

$$U_{Ld} = \frac{A_r\, U_{Lr}}{A_d} \quad (4)$$

The riser and downcomer diameter were 0.094 m and 0.039 m, respectively. The velocity of circulating liquid increased in the downcomer compared to the riser section in EXL ALFR.

3.3. Particle Image Velocimetry

PIV is a very sophisticated non-intrusive flow visualization method. Hollow glass silver-coated particles (12 µm, 1.03 g/cc) are put into the flow to mimic the flow to follow the behavior and reflect the laser. A laser Nd: YAG LASER (λ=532 nm) was used. When a laser is fired, an optical slit converts the beam into a laser sheet. The laser sheet illuminates the seeding glass particles. A synchronizer synchronizes the camera sensor to simultaneously expose the sensor and capture the image when a laser is fired through it. The camera details are as follows: Nikkor 135 mm, f/1.8 lens, TSI Power View 4M Plus Sensor, and $\Delta t \approx 200$ µs.

Insight 4G application was utilized for image processing to determine the local velocities in the interrogation region. A schematic of PIV is shown in Fig. 2. The liquid axial velocity was measured in the downcomer section below H = 400 mm from the gas-liquid separator. The shape of the downcomer section was a circular pipe distortion of images caused by the column curvature. The downcomer pipe over a rectangular box avoided the curvature effect. The rectangular box had a square cross-section (W×D) of 0.050 × 0.050 m^2 and a height (L) of 0.15 m. The gap between the downcomer pipe and the rectangular box was filled with water. The value of the refractive index of water and acrylic pipe was 1.33 and 1.495. Sodium iodide was used to adjust the refractive index of water. The liquid axial velocity was measured in EXL ALFR and EXL ALFR-

PB for superficial gas velocity ranging from 0.02 m/s to 0.10 m/s.

3.4. Bubble Size Distribution (BSD)

In the photographic method, the photos were taken with a high-definition camera (CANON1100D) in a single plane. A rectangular vessel was used to avoid optical reflections from the wall of the riser section. The bubble sizes were computed in a single rectangular plane for a height to diameter ratio ranging from 8.5 to 8.96 in the EXL ALFR and EXL ALFR with a fixed bed. A web plot digitizer was used for the bubble size. For a given hydrodynamic condition, 30 to 50 bubbles were selected, and their diameters were estimated.

4. Mathematical modeling

CFD provides detailed flow patterns in the EXL ALFR and EXL ALFR-PB, which helps understand the mixing patterns and configuration optimization. Previous CFD studies on EXL ALFRs were mainly applied to investigate the flow pattern, mixing time, gas hold-up, and axial dispersion coefficient [12] for the local hydrodynamics in their risers [64]. Momentum transfer in two-phase flow has been explained by Sato et al. [65]. In the present investigation, the CFD simulation of EXL ALFR and EXL ALFR-PB was carried out using a standard k-ε model. The simulations were carried out at different V_G using the finite element approach. Multiphase modeling was carried out using the Eulerian approach. The set of equations for multiphase systems has been given in earlier literature (11, 66-78).

5. Population balance model

The type of flow in an airlift reactor with external loop with a fixed bed is a polydisperse multiphase flow. A population balance equation must be formulated to deal with this flow type. The MUSIG (Multiple Size Group) models have been developed to handle polydispersed multiphase flows. The number density of particles of mass m is represented by n(v,t).

$$\frac{\partial}{\partial t}n(m,t)+\frac{\partial}{\partial x^i}\left(U(m,t)\,n(m,t)\right)=B_B-D_B+B_C+D_c \quad (5)$$

The birth, death, and coalescence rates are represented by $B_B,\ DB, D_B,$ and D_C, respectively.

The multiple size group models are discretized in Eq. (5) into size groups or bins. Eq. (5) is discretized into seven size groups in this study.

$$\frac{\partial(\rho_i\, r_i)}{\partial t}+\frac{\partial}{\partial x^i}(U_i\rho_i\, r_i)=S_i \quad (6)$$

The volume fraction, $f_i=\frac{r_i}{\epsilon_G}=\frac{n_iV_i}{\epsilon_G}$, where r_i is equivalent radius, ϵ_G is the gas hold up, n_i is the number density of size group i and Vi is the volume of bubble group i.

Eq. (6) may also be written as:

$$\frac{\partial}{\partial t}(\rho_i\,\epsilon_G\,f_i)+\frac{\partial}{\partial x^i}(U_i\,\rho_i\,\epsilon_G\ f_i)=S_i \quad (7)$$

The MUSIG model is used for writing the size fraction equation.

$$\frac{\partial}{\partial t}(\rho_d\,\epsilon_G\,f_i)+\frac{\partial}{\partial x^i}(\rho_d\,\epsilon_G\,U_d\,f_i)=S_i \quad (8)$$

5.1 Bubble Break-up Model (Luo and Svendsen Model)

The model developed by Luo and Svendsen is based on isotropic turbulence and probability theory and contains no unknown or adjustable parameters. Break-up kernels are often expressed as a function of the break-up fraction:

$$f_{BV}=\frac{m_j}{m_i}=\frac{{d_j}^3}{d^3}=\frac{{d_j}^3}{{d_j}^3+{d_i}^3} \quad (9)$$

where d_j and d_i are the diameters of the daughter bubbles in the binary breakage of a parent bubble with diameter d. The value interval of the breakage volume fraction is between 0 and 1.

$$g(m_i;f_{BV}m_i)=0.923F_B(1-\epsilon_G)\left(\frac{\varepsilon}{d_i^2}\right)^{1/3}\int_{\xi_{min}}^{1}\frac{(1+\xi)^2}{\xi^{11/3}}e^{-x}\,d\xi \quad (10)$$

where

$$x=\frac{12\left(f_{BV}^{2/3}+(1-f_{BV})^{2/3}-1\right)\sigma}{\beta\rho_L\varepsilon^{2/3}d_i^{5/3}\xi^{11/3}} \quad (11)$$

where ξ is the dimensionless size of its eddies in the inertial subrange of isotropic turbulence. The lower limit of the integration is given by:

$$\zeta_{min}=\frac{ER_{min}\eta}{d_i} \quad (12)$$

where

$$\eta=\left(\frac{1}{\varepsilon}v_c^3\right)^{1/4} \quad (13)$$

where ER_{min} is the minimum eddy ratio with the values between 11.4 and 31.4 (defaults to 11.4). In addition, F_B is a calibration coefficient, $\beta=2.047$, ε is the continuous-phase eddy dissipation

rate, $\nu_c$is the continuous-phase kinematic viscosity, and $\sigma$is the surface tension coefficient (0.923 and 2.0 from literature) [79]. The contribution of the birth rate due to the break-up of larger particles and the death rate due to breaking up into smaller particles to the source term is given in the above equations. The difference between birth rate and the death rate has become zero for the overall size groups given by Eq. (14).

$$\sum_i (B_{Bi} - D_{Bi)} = 0 \tag{14}$$

5.2 Bubble Coalescence Model (Prince and Blanch Model)

According to the model developed by Prince and Blanch, the coalescences of a pair of bubbles is a three-step process. First, the bubble strikes the liquid between them, then the liquid film drains until the film reaches a critical thickness. Lastly, the film ruptures and bubbles merge.

The coalescence kernel is thus governed by the collision rate of two bubbles and a collision efficiency relating to the time required for coalescence:

$$Q(m_i ; m_j) = (\theta_{ij}^T + \theta_{ij}^B + \theta_{ij}^S)\eta_{ij} \tag{15}$$

The collision efficiency is modeled by comparing the time required for coalescence t_{ij} with the actual contact time during the collision τ_{ij} :

$$\eta_{ij} = e^{-t_{ij}/\tau_{ij}} \tag{16}$$

$$t_{ij} = \left(\frac{\rho_L r_{ij}^3}{16\sigma}\right)^{1/2} \ln\left(\frac{h_o}{h_f}\right) \tag{17}$$

$$\tau_{ij} = \frac{r_{ij}^{2/3}}{\varepsilon^{1/3}} \tag{18}$$

where h_o is the initial film thickness, h_f is the critical film thickness when rupture occurs, and r_{ij} is the equivalent radius:

$$r_{ij} = \left(\frac{1}{2}\left(\frac{1}{r_i} + \frac{1}{r_j}\right)\right)^{-1} \tag{19}$$

The turbulent contributions to collision frequency are modeled as:

$$\theta_{ij}^T = F_{CT} S_{ij} \left(u_{ti}^2 + u_{tj}^2\right)^{1/2} \tag{20}$$

where the cross-sectional area of the colliding particles is defined by:

$$S_{ij} = \frac{\pi}{4}(d_i + d_j)^2 \tag{21}$$

The turbulent velocity is given by:

$$u_{ti} = \sqrt{2}\varepsilon^{1/3} d_i^{1/3} \tag{22}$$

and F_{CT} is a calibration factor. The buoyancy contribution to collision frequency is modeled as:

$$\theta_{ij}^B = F_{CB} S_{ij} |U_{rj} - U_{ri}| \tag{23}$$

where

$$U_{ri} = \sqrt{\frac{2.14\,\sigma}{\rho_L\, d_i} + 0.505\, g\, d_i} \tag{24}$$

and F_{CB} is a calibration factor. The shear contribution to collision frequency is currently neglected.

$$\sum_i (B_{Ci} - D_{Ci}) = 0 \tag{25}$$

By definition of interfacial area aij for the gas-liquid flow through the riser section in an airlift reactor with external loop with fixed bed can be determined through the relationship

$$a_{ij} = \frac{6\epsilon_G}{d_s} \tag{26}$$

where dS is the Sauter mean bubble diameter. The local Sauter mean bubble diameter is obtained from

$$d_s = \frac{1}{\sum_i \frac{f_i}{d_i}} \tag{27}$$

The interfacial area aij and the Sauter mean bubble diameter in Eq. 27 are important parameters that link the interaction between the liquid and gas phases.

6. Numerical implementation

The simulations were carried out as a steady-state flow pattern in EXL ALFR and EXL ALFR-PB using commercial software ANSYS CFX 14.0. For degassing, the boundary condition was employed for the outlet. The top surface of the reactors was made in such a way that only gas was allowed to escape the reactor. A no-slip boundary condition appeared at the reactor wall. The initial liquid was stagnant, and a volume fraction of air was zero in the computational domain. The air volume fraction at the inlet boundary was unity at the computational domain, while the inlet gas velocities were set to be 3.9, 7.8, 11.78, 15.70, and 19.63 m/s. The convergence criteria for all transport equations were set as 1x10-4. The Reynolds stress model was employed in the present simulation. A summary of previous work on CFD-PBM in a gas-

liquid flow in a bubble column and airlift reactor with external loop is given in Table 1. Several simulations were carried out for the grid independence and bin sensitivity studies to reduce computation costs and times.

Table 1. Summary of previous work on the simulation of gas-liquid flow in a reactor implementing a population balance model

Author/ Year	Reactor	Geometry (mm)	Superficial velocities (m/s)	Turbulence model	CFD code	Approach	Method	Interfacial Forces/Models	Coalescence Model	Breakage model
Lu et al.(2019) [27]	External loop airlift reactor	D_r = 50 D_d = 200	U_G = 0.010 to 0.040	k-ε standard	ANSYS Fluent 16.0	Euler -Euler	-	C_D - Schiller Naumann - Tomiyama - DBS local drag model C_L - Tomiyama C_{VM} - 0.5	Luo and Svendsen	Luo and Svendsen
Ekambara and Joshi (2008) [81]	Bubble column reactor	D = 150	U_G = 0.020	k-ε RSM	ANSYS-CFX-10.0.	Euler -Euler	MUSIG	C_D - Shii-Zuber C_L - Tomiyama C_{TD} - 0.5 C_{VM} - Negligible C_{WL} - Antal	Prince and Blanch	Luo and Svendsen
Swiderski et al., (2016) [82]	Bubble column reactor	D = 200 L = 1800	U_G = 0.0275 - 0.1130	k-ε	Trans AT	-	-	C_D - Tomiyama C_L - Tomiyama C_{WL} - Antal	Coulaloglou and Tavlarides	Laakkonen
Silva et al., (2011) [28]	External Loop airlift reactor	D_r = 230 D_d = 190	U_G = 0.05 – 0.08	k-ε	ANSYS CFX 11.0	Euler -Euler	MUSIG	C_D - Shii-Zuber C_L- Negligible C_{TD} - Negligible C_{VM} - Negligible C_{WL} - Negligible	Prince and Blanch	Luo and Svendsen
Law and Battaglia (2013) [30]	External Loop airlift reactor	D_r = 102 D_d = 25	U_G = 0.01 – 0.2	k-ε standard	ANSYS CFX	Euler -Euler	-	C_D - Schiller Naumann C_{VM} - 0.5	Prince and Blanch	Luo and Svendsen
Wang and Sun (2009) [83]	Bubble column Reactor	D = 50.8 L = 3060	U_G = 0.028 - 0.321 U_L= 0.491 - 0.986	k-ε standard	Fluent 6.2.16	Euler -Euler	IATE	C_D - Tomiyama C_L - 0 and 0.29	Yao and Morel	Yao and Morel
Cheung et al., (2007) [84]	Bubble column Reactor	D = 50.8 L = 3061	U_G = 0.0473 - 0.242 U_L = 0.491 - 0.986	k-ω SST	Ansys CFX-11	-	MUSIG	-	Prince and Blanch	Luo and Svendsen
Frank et al., (2008) [85]	Bubble column reactor	D = 51.2 L = 4000 D = 194	U_G = 0.0040 - 0.0368 U_L = 0.225 - 1.611	k-ω SST	Ansys CFX-10	Euler -Euler	MUSIG	C_D - Grace and Tomiyama C_L - Tomiyama C_{WL} - Antal, Tomiyama, Frank C_{TD} - Burns	Prince and Blanch	Luo and Svendsen

Author/ Year	Reactor	Geometry (mm)	Superficial velocities (m/s)	Turbulence model	CFD code	Approach	Method	Interfacial Forces/Models	Coalescence Model	Breakage model
Krepper et al., (2008) [86]	Bubble column reactor	D = 51.2 L = 3300	U_G = 0.14 - 0.2194 U_L = 1.017	-	Ansys CFX-4	Euler -Euler	MUSIG	C_L - Tomiyama	Prince and Blanch	Luo and Svendsen
Podila et al., (2007) [87]	Bubble column reactor	-	U_G = 0.113 U_L = 0.98	k-ε	Fluent-6.3.26	Euler -Euler		C_D - Ishii-Zuber, Rushe and Issa C_L - Troshko C_{TD} - Violet and Simonin C_{VM} - 0.5	Prince and Blanch, Luo, Lehr	Luo and Svendson Lehr
Huh et al., (2006) [88]	Pipe	D = 80 L = 10000	U_G = 0.1 - 0.698 U_L = 0.5 - 2	-	-	-	-	-	Prince and Blanch,	Prince and Blanch,
Lo and Zhang (2009) [89]	Pipe	D = 50.8 L = 3060	U_G = 0.321 - 0.624 U_L = 0.986 - 2.01	k-ε standard	STAR-CD 3.27	Euler -Euler		C_D - 1.017 C_L - (-0.2888) C_{VM} - 0.5	The newly proposed Sγ model	The newly proposed Sγ model
Present work	**Airlift reactor with external loop with a fixed bed**	**D_r = 94 D_d = 47**	**U_G = 0.02 to 0.10**	**k-ε RSM**	**ANSYS CFX 14**	**Euler -Euler**	**MUSIG**	**C_D - Grace C_L - Tomiyama C_{TD} -Tomiyama, C_{VM} - 0.5 C_{WL} - Antal**	**Prince and Blanch**	**Luo and Svendsen**

6.1 Bin Sensitivity study

The PBM indicates that the bubble size ranges from 1 to 15 mm in diameter. For the present work, a bin sensitivity study was carried out. The bubbles were equally divided into 5, 7, and 10 size groups. In this case, the equal diameter discretization was adopted. The diameter represented by group i is calculated from:

$$d_i = d_{min} + \Delta d\left(i - \frac{1}{2}\right) \quad (28)$$

where d_{min} is the minimum bubble diameter, and

$$\Delta d = \frac{d_{max} - d_{min}}{N} \quad (29)$$

where d_{max} is the maximum bubble diameter and N is the number of groups. The computational results were all based on the discretization of the 7 bubble size groups. The Multiple Size Group (MUSIG) model was employed with discrete bubble sizes arranged in the disperse phase. Each bubble was tracked by solving an additional seven transport equations. The following (Eq. 30) size of the bubbles was generated at the sparger reported in the literature [80]. The sparger had five openings; each hole became 3 mm in diameter.

$$d_b = \left(\frac{6\,\sigma\,d_s}{g\,(\rho_l - \rho_g)}\right)^{1/3} \quad (30)$$

The calculated diameter of d_b = 5.1 mm was thus the size fraction of the 3rd bubble group with a diameter of 4.28 to 6.42 mm set to be unity for the inlet condition.

6.2 Computational Grid

The geometrical dimensions of EXL ALFR and EXL ALFR-PB were explained in the previous section. The MATLAB code was written for the insertion of the packing in the downcomer. The code was read in GAMBIT workbench Ansys 14. The insertion of the packing in the downcomer is shown in Fig. 3. The property of packing was discussed in Section 3. The

CFD geometry view of the airlift reactor with external loop with and without packing is shown in Fig. 3. The three grid sizes were (Grid-1) 2.8 million, (Grid-2) 3.15 million, and (Grid-3) 2.1 million.

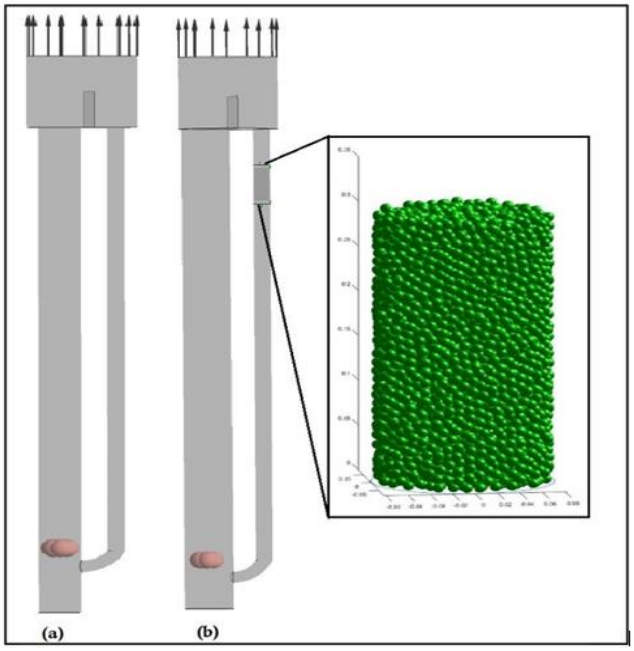

Fig. 3. Geometrical view of airlift reactor with external loop and airlift reactor with external loop with a fixed bed.

The liquid axial velocity was determined in a downcomer at height H = 400 mm for a superficial gas velocity of 0.04 m/s for the different grid sizes. From experimental and CFD simulations, the liquid axial velocity was determined for different grid sizes. The liquid axial velocity from the experimental PIV was investigated. Fig. 4 shows that grid size 2.8 million and 3.15 million showed closer results of experimental liquid axial velocity.

From the CFD simulation, in comparison with different grids, Fig. 4 depicts that grid sizes 2.8 million and 3.15 million showed similar results of liquid axial velocity. Hence, 2.8 million grids were adapted for further simulations.

The present work continues the grid size of 2.8 million for further simulations. The liquid axial velocity from the experiment was obtained from a PIV instrument converted into a contour plot. It seemed to be CFD post-processing results. The MATLAB code was written to convert PIV liquid axial velocity results into contour plots in color images, as shown in Fig. 5. For the predicted and experimental sample contours of liquid axial velocity in the downcomer in EXL ALFR-PB for superficial gas velocity, 0.04 m/s is shown in Fig. 5. It can be seen in Fig. 5 that the experimental and CFD contour of liquid axial velocity was nearly the same. The liquid axial velocity was more at the centre of the downcomer and less near the wall of the downcomer, as observed in Fig. 5.

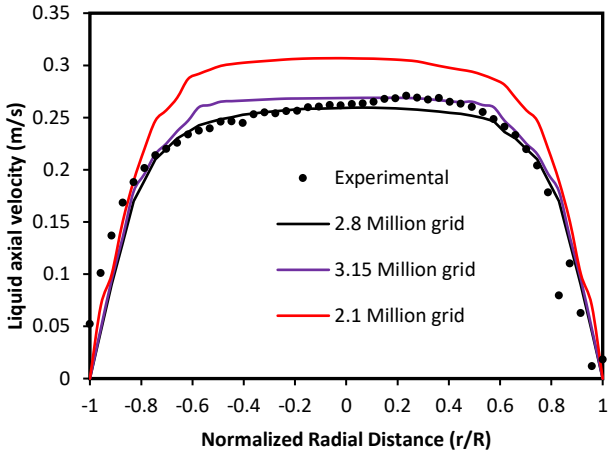

Fig. 4. Experimental and simulation result of liquid axial velocity in downcomer for superficial gas velocity 0.04 m/s for different grid sizes.

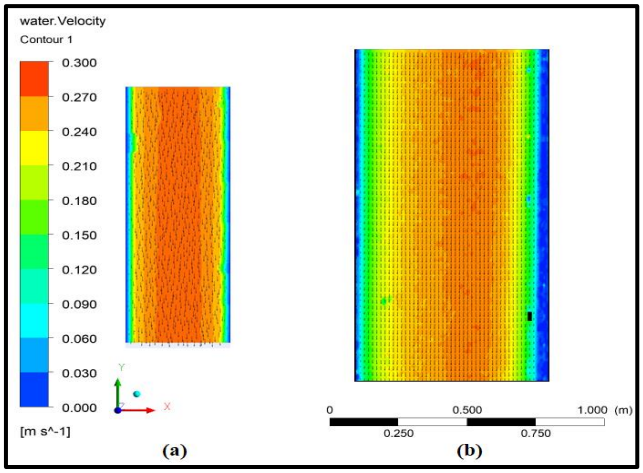

Fig. 5. Contours of axial liquid velocity in downcomer in EXL ALFR-PB for superficial gas velocity 0.04 m/s (a) Predicted (b) Experimental.

7. Results and discussion

The experiment was conducted for EXL ALFR and EXL ALFR-PB over a wide range of superficial gas velocities. The CFD simulations were carried out using the RSM-PBM model with BSD for a range of superficial gas velocities (0.02 m/s to 0.10 m/s) to compare with the experiment for the external loop airlift and external loop airlift with fixed bed reactor (EXL ALFR-PB). The hydrodynamic data in

the reactors were obtained using an air/water system. The hydrodynamic parameters of the overall gas hold-up, velocity of circulating liquid, Saunter mean bubble diameter, and liquid axial velocity in the downcomer (H=400 mm) pressure drop across the fixed bed were estimated. The radial profile of liquid axial velocity at a location in the downcomer (H=400 mm) was measured for a superficial gas velocity of 0.02 to 0.10 m/s. The liquid axial velocity in EXL ALFR and EXL ALFR-PB was compared for the same superficial gas velocity. The experimental from the PIV radial profile of liquid axial velocity was compared with the predicted from the population balance model.

7.1 Gas hold-up (ϵ_G)

Studies on this aspect are reported in the literature [65,90]. The parameters C_O and C_1 are the drift-flux constants found in EXL ALFR and EXL ALFR-PB compared to the literature reported values. For the present study, the drift-flux constants were determined for EXL ALFR and EXL ALFR-PB, and the slip velocity vs. total gas-liquid velocity was studied.

$$* \ \mathrm{LHS} = \frac{U_G}{\epsilon_G}; \quad \mathrm{RHS} = C_O(U_G + U_L) + C_1; \tag{31}$$

The material balance was done for EXL ALFR and EXL ALFR-PB, as shown in Table 2. The overall gas hold-up with the UG in EXL ALFR and EXL ALFR-PB is shown in Fig. 6. This unfolds three different flow regimes: (i) a homogeneous bubbly flow. The hold-up increased continuously; the bubbles rose individualistically without merging when gas velocity increased in homogeneous bubbly flow. This regime existed over the approximate superficial gas velocity range U_G > 0.01 m/s; (ii) a transition flow regime existed over the gas velocity range where the bubbly flow developed into a heterogeneous flow. It can be seen from Fig. 6 that the slope of the line changed after a superficial gas velocity of 0.05 m/s. The slip velocity from the experimental data was plotted against the total gas-liquid velocity. The Zuber and Findlay's drift flux plot was not linear; it was a changing slope at total gas-liquid velocity (U_G + U_{Lc}) = 0.42 m/s; and (iii) the fully developed heterogeneous flow (U_G > 0.05 m/s) is shown in Fig. 6. When the coalescence was well authorized, the hold-up again increased strongly According to the drift flux model, gas flowrate increased because of the evolution of large `spherical cap' bubbles.

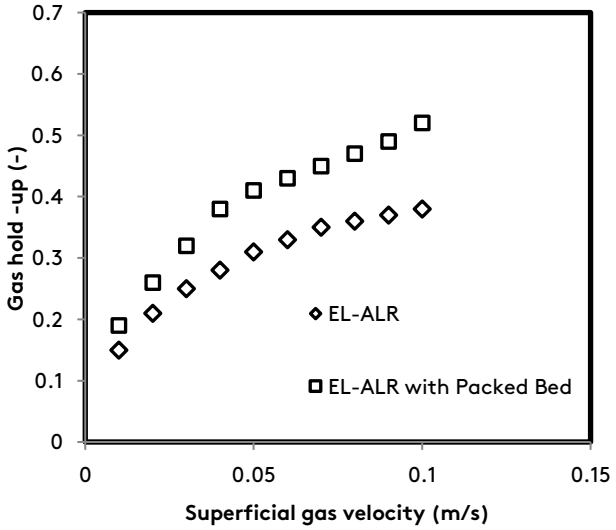

Fig. 6. Comparison of experimental gas hold-up vs. superficial gas velocity for EXL ALFR and EXL ALFR-PB.

With the implementation of the CFD-PBM model, air volume fraction contours were observed for both reactor cases, as shown in Figs. 7 and 8. A higher air volume fraction was observed in EXL ALFR-PB than in EXL ALFR for the same operating condition: U_G at 0.02 to 0.10 m/s. The velocity of circulating liquid in EXL ALFR-PB was less than EXL ALFR for the same operating condition. The packing was fixed in the downcomer section. The voidage of packing was 0.67, and the packing height was 0.1 m.

The particle diameter was 0.0043 m, and the sphericity was 0.87. The experiment was performed in semi-batch mode. The water was already filled in a reactor the gas passed at the bottom sparger. When gas was sparged in the riser section, slip velocity between the gas and liquid existed. The velocity of the circulating liquid was less in the EXL ALFR-PB due to the packing, causing resistance to the water flow in the downcomer section. The packing resistance depended on the void fraction and sphericity of the packings. The bubble rise velocity was also less in the riser section for the same operating condition. Thus, the gas hold in EXL ALFR-PB increased with superficial gas velocity, as shown in the Fig. 8 contours from the CFD simulation. The experimentally determined gas hold-up and CFD prediction of gas hold for both reactor cases were in good agreement, as shown in Fig. 13.

Table 2. Material balance for EXL ALFR and EXL ALFR-PB.

						Material balance*	
Reactors	**Superficial gas velocity (U_G) m/s**	**Superficial liquid velocity (U_L) m/s**	**Gas hold up (ϵ_G)**	$\frac{U_G}{\epsilon_G}$	$U_G + U_L$	**LHS**	**RHS**
External loop airlift reactor	0.01	0.15	0.15	0.067	0.16	0.067	0.073
	0.02	0.20	0.21	0.095	0.22	0.095	0.089
	0.03	0.25	0.25	0.12	0.28	0.120	0.105
	0.04	0.32	0.28	0.143	0.36	0.143	0.126
	0.05	0.37	0.31	0.161	0.42	0.161	0.142
	0.06	0.48	0.33	0.182	0.54	0.182	0.173
	0.07	0.59	0.35	0.200	0.66	0.200	0.205
	0.08	0.68	0.36	0.222	0.76	0.222	0.232
	0.09	0.75	0.37	0.243	0.84	0.243	0.253
	0.10	0.80	0.38	0.263	0.9	0.263	0.269
Airlift reactor with external loop with a fixed bed	0.01	0.08	0.19	0.053	0.09	0.053	0.065
	0.02	0.12	0.26	0.077	0.14	0.077	0.081
	0.03	0.15	0.32	0.094	0.18	0.094	0.094
	0.04	0.16	0.38	0.105	0.20	0.105	0.10
	0.05	0.19	0.41	0.122	0.24	0.122	0.113
	0.06	0.24	0.43	0.14	0.30	0.140	0.132
	0.07	0.29	0.45	0.156	0.36	0.156	0.151
	0.08	0.34	0.47	0.17	0.42	0.170	0.170
	0.09	0.38	0.49	0.184	0.47	0.184	0.186
	0.10	0.42	0.52	0.192	0.52	0.192	0.202

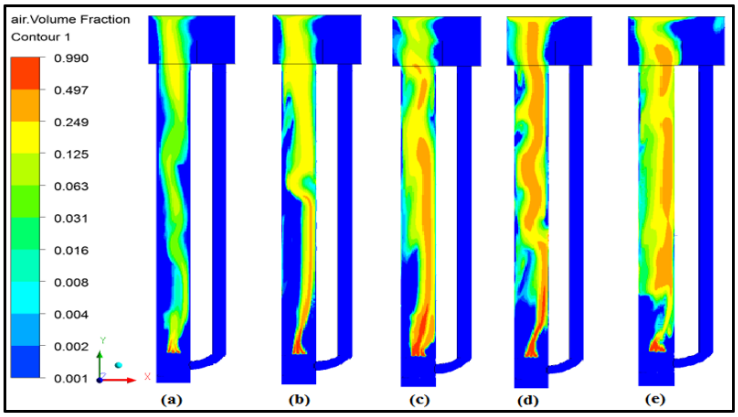

(a) U_G = 0.02 m/s (b) U_G = 0.04 m/s (c) U_G = 0.06 m/s (d) U_G = 0.08 m/s (e) U_G = 0.10 m/s

Fig. 7. Air volume fraction contours in EXL ALFR for superficial gas velocity.

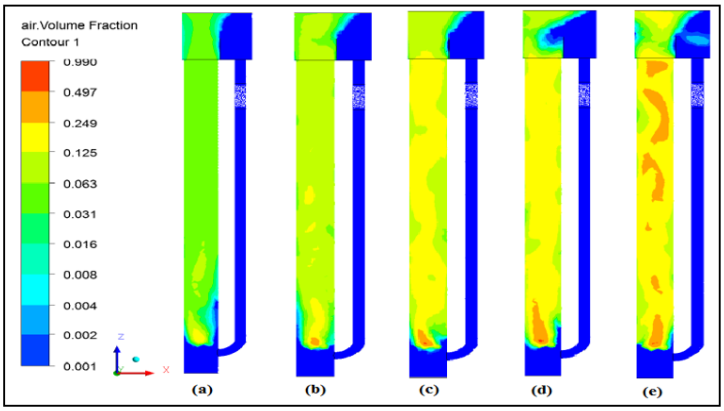

(a) U_G = 0.02 m/s (b) U_G = 0.04 m/s (c) U_G = 0.06 m/s (d) U_G = 0.08 m/s (e) U_G = 0.10 m/s

Fig. 8. Air volume fraction contours in EXL ALFR-PB for superficial gas velocity.

7.2. Velocity of circulating liquid (U_L)

The gas was introduced in the riser section through the sparger. The air bubble spontaneously moved upward at a certain rise velocity of air bubbles. According to Stokes law, the rise velocity of air bubbles depends on bubble size, viscosity, and density difference between the working fluid and air. The liquid circulation pattern is quickly established due to air bubbles in the riser section, and the fluid density becomes less than the downcomer section fluid. The velocity of circulating liquid is one of the most significant parameters for airlift reactors' proper design and operation. The effect of the superficial gas velocity (U_G) on the velocity of circulating liquid for EXL ALFR and EXL ALFR-PB is shown in Fig. 9. The velocity of the circulating liquid was a characteristic parameter of the EXL ALFR. The velocity of the circulating liquid dictated the efficient performance of EXL ALFR. It was observed that the velocity of the circulating liquid was strongly dependent on the superficial gas velocity. The reduced density in the riser section rapidly pulled the liquid from the downcomer, and the liquid circulations were established.

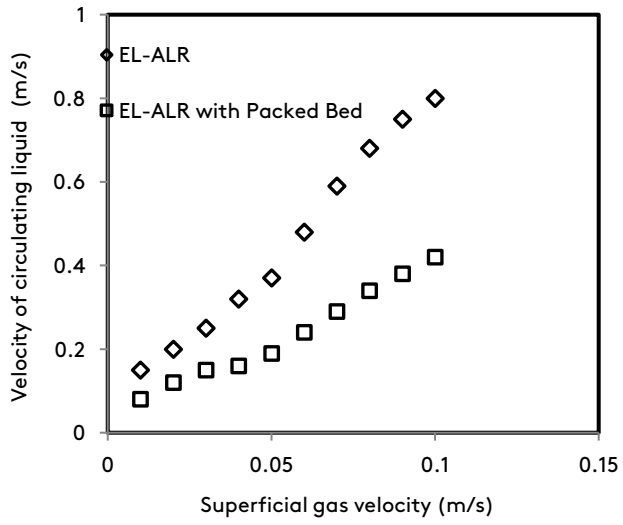

Fig. 9. Experimental velocity of circulating liquid vs. superficial gas velocity for EXL ALFR and EXL ALFR-PB.

The riser section is just like a conventional bubble column, an initial homogeneous bubbly flow pattern with uniform hold-up distribution in the domain at lower gas superficial velocities transits into the transition regime. The bubbles coalesce to form bigger bubbles, which travel at faster velocities. Also, coalescence causes a reduction in an interfacial area, which in turn reduces the exchange of momentum between the phases. As shown in Fig. 6, the value of average gas hold-up was a linear change with superficial gas velocities from 0.01-0.04m/s. Hence, the velocity of the circulating liquid increased less rapidly in the transition regime. The heterogeneous regime was established after sufficiently higher superficial gas velocity, giving a hold-up distribution across the flow domain.

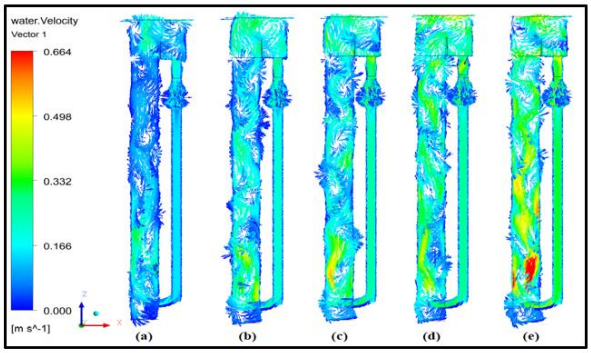

(a) $U_G = 0.02$ m/s **(b)** $U_G = 0.04$ m/s **(c)** $U_G = 0.06$ m/s **(d)** $U_G = 0.08$ m/s **(e)** $U_G = 0.10$ m/s

Fig. 10. Water velocity vector in EXL ALFR-PB for superficial gas velocity.

It can be seen in Fig. 6 and Fig. 9 that the gas hold-up and the velocity of circulating liquid increased at more stable rates after a superficial gas velocity of 0.06 m/s. The CFD simulation compared the water velocity vectors for U_G from 0.02 to 0.10 m/s in EXL ALFR and EXL ALFR-PB, as shown in Figs. 10 and Fig.11. Thus, water velocity in the downcomer leg of EXL ALFR was higher than the EXL ALFR-PB in the same operating condition.

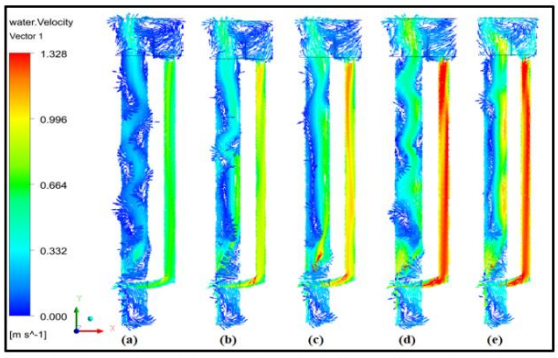

(a) $U_G = 0.02$ m/s **(b)** $U_G = 0.04$ m/s **(c)** $U_G = 0.06$ m/s **(d)** $U_G = 0.08$ m/s **(e)** $U_G = 0.10$ m/s

Fig. 11. Water velocity vector in EXL ALFR for superficial gas velocity.

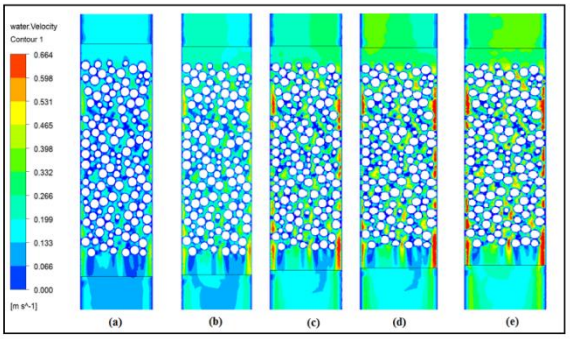

(a) $U_G = 0.02$ m/s **(b)** $U_G = 0.04$ m/s **(c)** $U_G = 0.06$ m/s **(d)** $U_G = 0.08$ m/s **(e)** $U_G = 0.10$ m/s

Fig. 12. Effect of superficial gas velocity on water circulation velocity contours in EXL ALFR-PB.

The flow in the downcomer section was significant for the proposed applications of EXL ALFR-PB. The velocity contours through the packed section for different gas superficial velocities are shown in Fig. 12. The liquid velocity contours indicated that in the packed section, as superficial gas velocity increased, liquid circulation increased; the local velocities in a packed section were more than two times the circulation velocities of liquid. Thereby, the intimate contacting of solid catalysts occurred with the liquid phase at higher velocities, which helped to increase the rate of reaction. The experimentally determined gas hold-up and velocity of circulating liquid in the riser section and CFD prediction for both reactor cases were in good agreement, as shown in Fig.13. The percentage error between the experimental and predicted results of the gas hold-up and the velocity of circulating liquid in EXL ALFR and EXL ALFR-PB was determined. The minimum percentage of errors were respectively 2.3% and 1.2%, and a maximum of 4.2% and 3.4% were determined for the experimental and predicted values of the gas hold-up in EXL ALFR and EXL ALFR-PB. The velocity of the circulating liquid for the predicted and experimental values of their minimum percentage error were respectively 1.1% and 0.5% and a maximum of 4.3% and 4.5% in EXL ALFR and EXL ALFR-PB.

7.3. Bubble Size Distribution (d_b)

Experiments were performed on a 1.35 m long vertical tube riser with a riser diameter of 0.094 m and a downcomer diameter of 0.039 m. The flow conditions were U_G = 0.02 to 0.10 m/s, and the gas volume fraction at the inlet was 12.1%. The simulations were performed in EXL ALFR and EXL ALFR-PB with a validated developed CFD model. Bin sensitivity analysis was done to predict BSD accurately. Bin 7 was continued for further simulation; the reason was explained in section 5.5.1. The size fraction of the 3rd bubble group with a diameter of 4.28 to 6.42 mm was set to be unity for the inlet condition. From the CFD simulation, the air mean bubble diameter was obtained for superficial gas velocity in EXL ALFR and EXL ALFR-PB, as shown in Fig. 14. The air mean bubble diameter difference was observed in both reactors for the same operating condition.

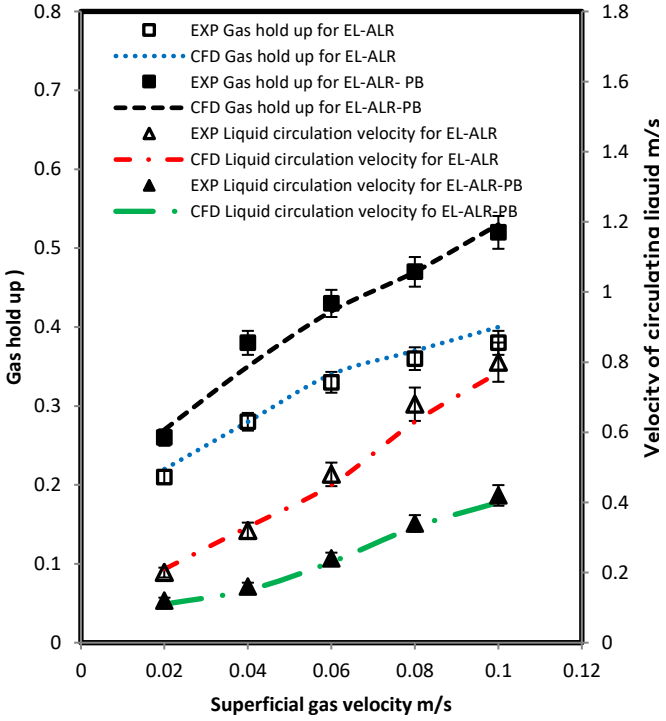

Fig. 13. Comparison of experimental and CFD prediction of gas hold-up and velocity of circulating liquid in riser section for EXL ALFR and EXL ALFR-PB.

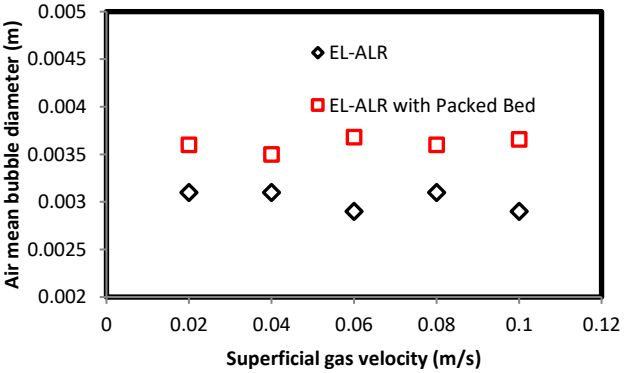

Fig. 14. Comparison of air mean bubble diameter in EXL ALFR and EXL ALFR with a fixed bed reactor.

The air mean BSD on an overall domain for different superficial gas velocities was observed from the simulation. In EXL ALFR, the near entry of sparger 0.0024 m sizes of bubbles was determined from the correlation for the superficial gas velocity from 0.02 to 0.10 m/s. The initial superficial gas velocity of 0.02 m/s for the large sizes of the bubbles was predicted from CFD simulation and experimental due to the coalescence of the bubbles. From Fig. 15a-e, bubble sizes above 0.0012 m were observed; bubbles having a lesser diameter than 0.0012 broke down to a smaller size. In Fig 15a-e, it can be observed that the homogeneous MUSIG model yielded significant BSDs for small and large bubble diameters in the EXL ALFR domain, indicating the presence of bubble break-up and coalescence. For the range of air mean bubble diameter (0.00214 m), the maximum percentage of bubbles was observed in the EXL ALFR domain for the superficial gas velocity from 0.02 to 0.10 m/s (Fig. 15a-e). The bubble coalescence dominated for the higher superficial gas velocity at 0.10 m/s, as shown in Fig.15e.

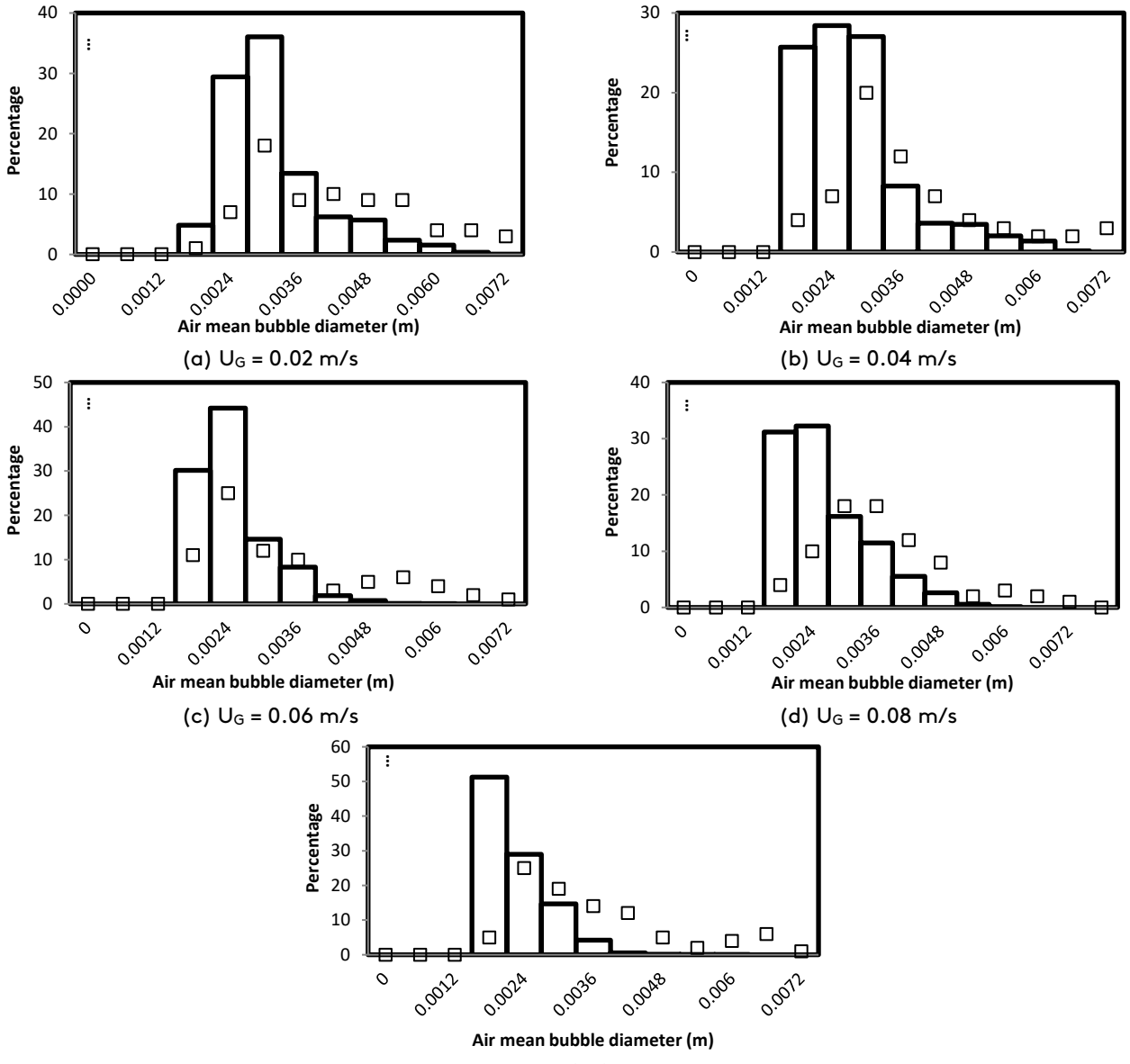

Fig. 15. BSD in the domain of airlift reactor with external loop for different superficial gas velocities for Experimental (□) and predicted (bins).

In EXL ALFR-PB, the gas hold-up was higher, and the velocity of circulating liquid was less for the same operating condition. Due to the lower velocity of the circulating liquid, the bubble residence time in the riser was higher. The bubbles spent more time in the riser section, so the overall gas hold-up increased. For the air mean bubble diameter from 0.001 to 0.00214m, an average of 50% was observed, and 5% to 10% of air mean BSD from 0.00428 to 0.01071m was also observed (Fig.16a-e). Large bubbles were generated in EXL ALFR-PB compared to EXL ALFR due to coalescence. The coalescence dominated in EXL ALFR-PB compared to EXL ALFR for the same operating condition. Due to the rise velocity of the bubbles being less in EXL ALFR-PB, the bubbles came closer to form big size bubbles. The liquid turbulence in EXL ALFR was higher than in EXL ALFR-PB for the same operating condition.

Fig.16b-e presents the bubble breakup and coalescence effect. Coalescence was dominating for the initial superficial gas velocity (U_G = 0.02 m/s), and for a superficial gas velocity from 0.04 to 0.10 m/s, we cannot predict. So, break up and coalescence are both present. The experimental BSD and prediction for CFD simulation had a good agreement, as shown in Fig. 15a-e and Fig. 16a-e. In Fig. 17, it can be observed that the model overestimated the bubble size near the sparger. The coalescence was the dominant phenomenon, only nearer the top region of the riser section.

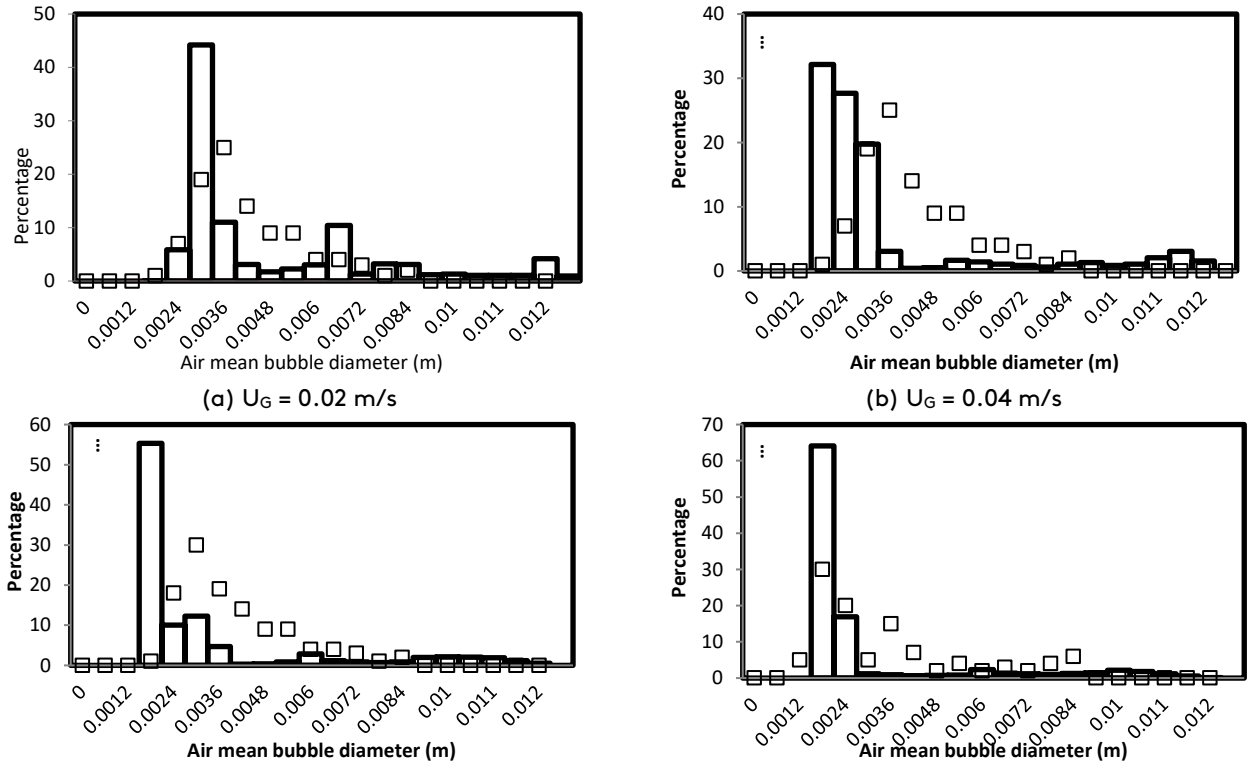

(a) U_G = 0.02 m/s

(b) U_G = 0.04 m/s

(c) U_G = 0.06 m/s

(d) U_G = 0.08 m/s

Fig. 16. BSD in the domain of external loop airlift with a fixed bed for different superficial gas velocity for Experimental (□) and predicted (bins).

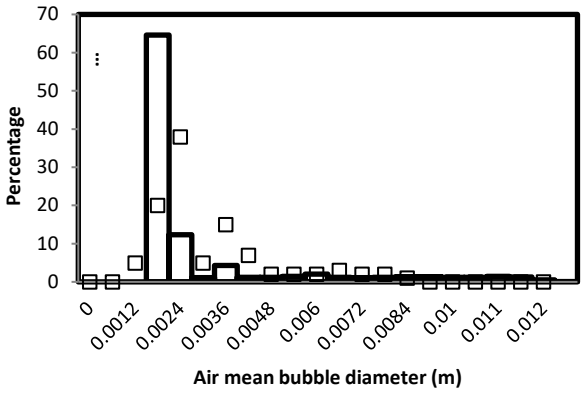

(e) U_G = 0.10 m/s

Fig. 16. Continued

Fig.17a-e shows that the bubble coalescence rate also increased with an increase in superficial gas velocity from 0.02 to 0.10 m/s. It was also observed that the local air mean bubble size in the central region was more significant than in the wall region in the riser section. Except near the wall region, the BSD was almost a constant cross-sectional area. For the BSD, in comparison with both reactors for the same operating condition, the average BSD was less (0.0012 to 0.006 m) in EXL ALFR compared to EXL ALFR-PB (0.0012 to 0.012 m), as shown in Figs. 15 and 16. The velocity of the circulating liquid was less due to the coalescing phenomenon occurring. The average bubble size generated in EXL ALFR was less than EXL ALFR-PB. The bubble coalescing phenomenon was observed at the top of the reactor from CFD simulation contours, as shown in Fig. 17. Small size bubbles were observed in the nearer sparger location, and big size bubbles were at the top.

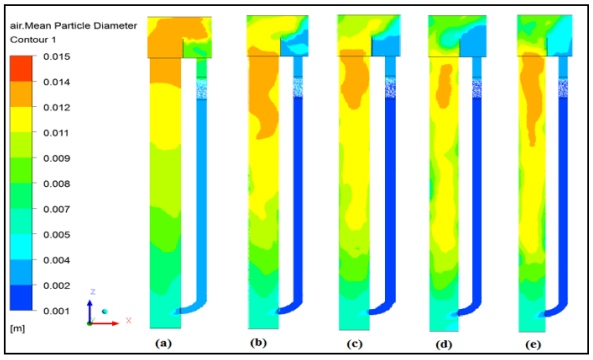

(a) U_G = 0.02 m/s (b) U_G = 0.04 m/s (c) U_G = 0.06 m/s (d) U_G = 0.08 m/s (e) U_G = 0.10 m/s

Fig. 17. Air mean bubble diameter in riser section EXL ALFR with fixed bed with different superficial gas velocity.

7.4 Liquid axial velocity in EXL ALFR and EXL ALFR with a fixed bed

PIV was used to measure the liquid axial velocities in the downcomer sections (H= 400 mm) for superficial gas velocity from 0.02 to 0.10 m/s, as shown in Fig. 2. PBM with RSM was used in the simulation and compared with the experimental and predicted results of liquid axial velocity. The sample contours of the axial liquid velocity in the downcomer in EXL ALFR-PB for a superficial gas velocity of 0.04 m/s for the predicted and experimental is shown in Fig. 5. The liquid axial velocity was measured and compared with both reactors at a superficial gas velocity from 0.02 to 0.10 m/s, as shown in Figs.18 and 19. The liquid axial velocity decreased in EXL ALFR-PB compared to EXL ALFR for the same operating condition. In the previous section, it can be seen from Fig. 9 that liquid circulation velocities decreased in EXL ALFR-PB compared to EXL ALFR due to internal packing. The velocity of the circulating liquid and axial velocity depended upon a void fraction of packing in the downcomer. Figs. 18 and 19 show the comparison of experimental and predicted axial liquid velocity for the RSM turbulent model with PBM. The RSM model with PBM better predicted the liquid axial velocity with the experimental results.

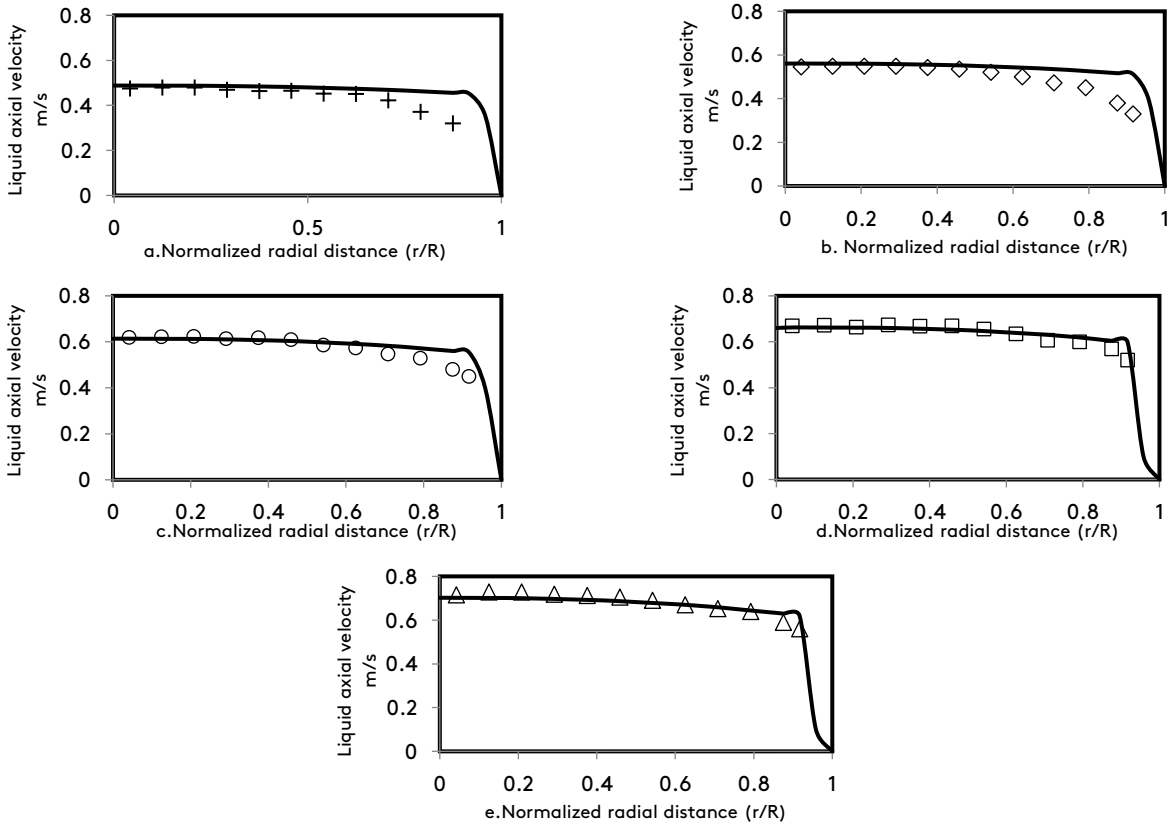

Fig. 18. Experimental and simulation result of liquid axial velocities in downcomer at height H = 400 mm for different superficial gas velocity in EXL ALFR (a) U_G = 0.02 m/s (+) (b) U_G = 0.04 m/s (◊) (c) U_G = 0.06 m/s (○) (d) U_G = 0.08 m/s (□) (e) U_G = 0.10 m/s (△).

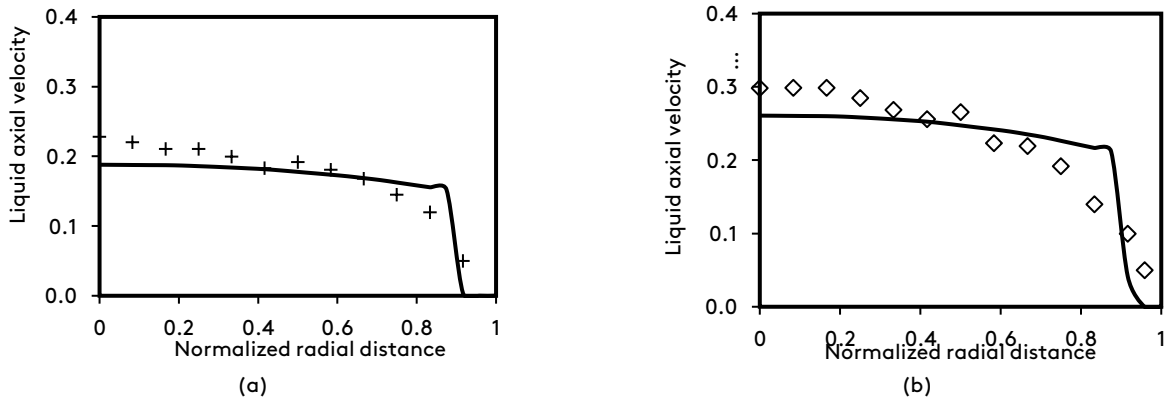

Fig. 19. Experimental and simulation result of liquid axial velocities in downcomer at height H= 400 mm for different superficial gas velocity in EXL ALFR-PB. (a) UG = 0.02 m/s (+) (b) UG = 0.04 m/s (◊) (c) UG = 0.06 m/s (○) (d) UG = 0.08 m/s (□) (e) UG = 0.10 m/s (△).

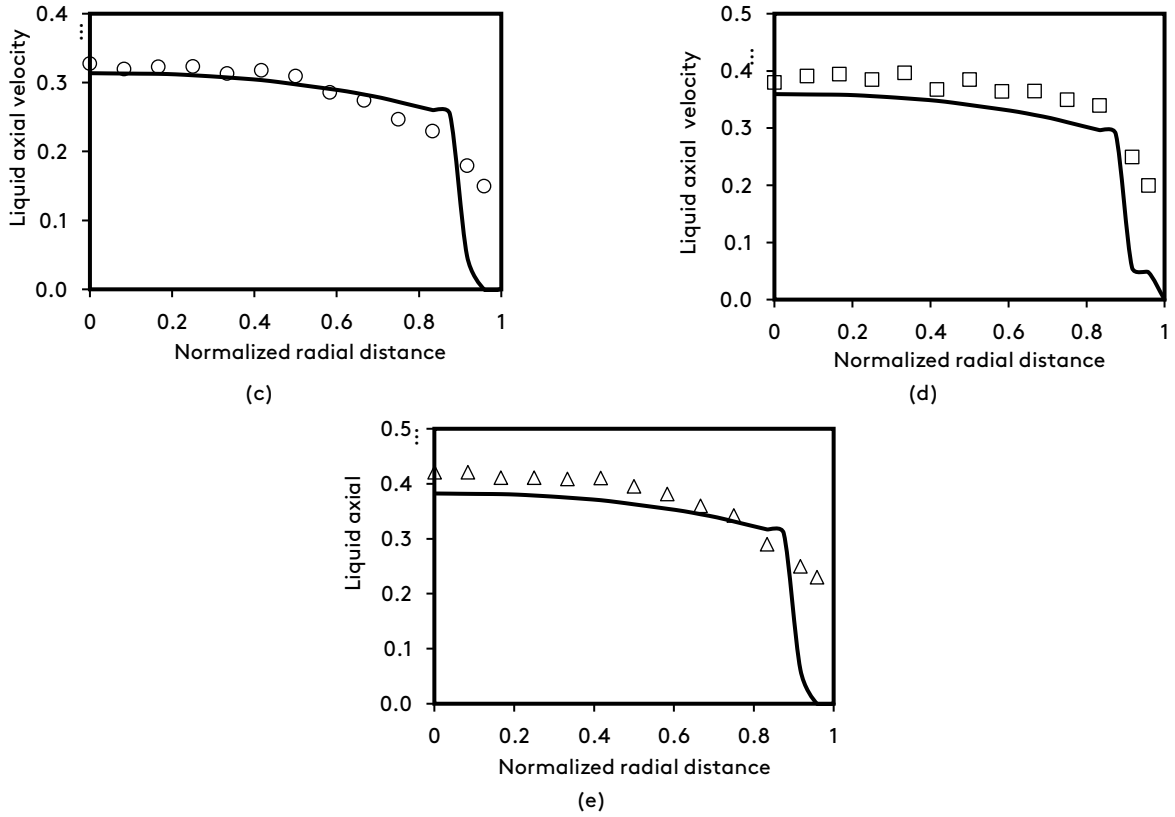

Fig. 19. Continued

7.5. Overall pressure drops (ΔP) and pressure drops across the bed (ΔP_B)

The pressure drop increased proportionally to the frictional shear forces within the EXL ALFR-PB. Pressure drop is an essential factor that influences the design and operation of EXL ALFR-PB. The effect of the superficial gas velocity (U_G) on pressure drop is shown in Fig. 20. The following Ergun equation determines the pressure drop across the fixed bed in the downcomer section in EXL ALFR.

$$\Delta P = \frac{150\mu\,(1-\epsilon)^2\,V_S\,L}{\epsilon^3\,D_p^2} + \frac{1.75\,(1-\epsilon)\rho V_S^2\,L}{\epsilon^2 D_p} \quad (32)$$

Covering a wide range of particle sizes and shapes presents a general equation to determine the pressure drop across a fixed bed for all flow conditions (laminar to turbulent) using a broad set of experimental data. The Ergun equation is commonly used for flow through a randomly fixed bed of spheres. The pressure drop is linearly related to superficial liquid velocity for the laminar flow regime. For turbulent flow regimes, pressure drop increases with the square of the superficial liquid velocity and linearly depends on fluid density. It can be seen from Fig. 20 that the predicted pressure drop across the fixed bed was in good agreement with the Ergun equation prediction. The overall pressure drop and pressure drop across the fixed bed depended on the flow resistance. The local liquid axial velocity and radial velocity for difference superficial gas velocity were affected due to internal packing, as shown in Fig. 12. The pressure drop across the bed was significantly more significant than the overall pressure in the reactor, and the resistance offered to the flow presence of packing. The present work voidage of packing was 0.67. The pressure drop across the bed depended on the voidage of packing. As it increased, the voidage of packing, velocity of circulating liquid, and axial velocity within the packing were also affected. Immobilized enzymes might be sensitive to shear stress. It can be seen from Fig. 21 that the share stress between the packing and liquid also increased with superficial gas velocity.

7.6. Turbulent Shear Stress (τ_s)

Airlift reactors are frequently used in biochemical engineering due to their simple construction and less shear stress imposed on the cells than the mechanically stirred tanks. The undesirable effects, like activity and structure degradation,

take place due to turbulent shear stresses. The proteins may deactivate due to shear stress; also, for the proteins deceiving at gas-liquid interface, the deactivation is enhanced by the presence of turbulent shear stress [91]. Turbulent shear stress was calculated from Eq. 33 for the present work.

$$\tau_s = \eta \frac{du}{dy} \quad (33)$$

where η and du/dy are the eddy viscosity and shear strain. Both these parameters are calculated from the CFD simulation for different superficial gas velocities. In the downcomer region in EXL ALFR-PB, maximum τ_s could be observed due to a fixed bed. It is indicated from Fig. 21 that τ_s increased with an increase in U_G ($\tau_s \propto U_G^{0.72}$). The maximum value of τ_s was around 4 Pa in the downcomer. With increased superficial gas velocity in the riser section, the velocity of circulating liquid was also grown in the fixed bed of the downcomer. The τs in the fixed bed of the downcomer was a function of the velocity of the circulating liquid. Conventional reactors (bubble columns, fluidized beds, and fixed bed reactors) have both gas-liquid-solid contacts in the reactor. The literature [91] has reported that gas bubbles in the system increase the interfacial force of the gas-liquid. This effect can be significantly enhanced under conditions where a gas-liquid interface occurs along with agitation.

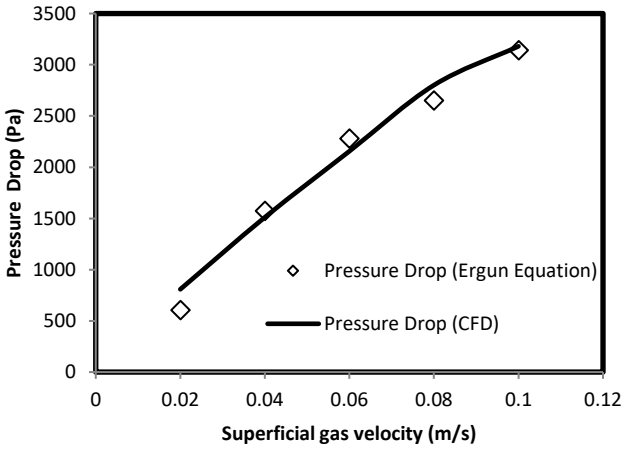

Fig. 20. Comparison of CFD simulation and Ergun equation of pressure drop vs. superficial gas velocity in EXL ALFR with a fixed bed.

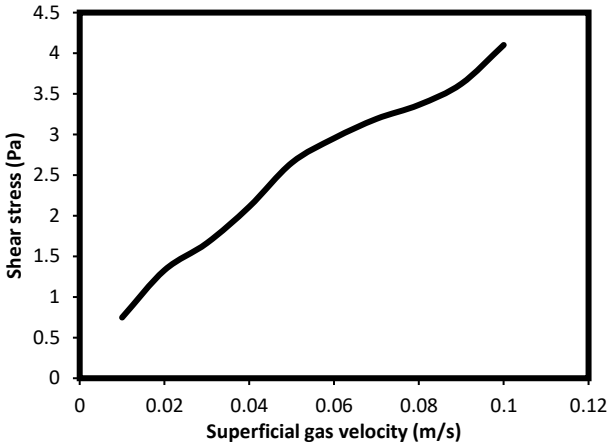

Fig. 21. CFD simulation shear stress vs. superficial gas velocity in EXL-ALFR-PB.

The shear stress depends on shear velocity with direct proportionality in a fixed bed in EXL ALFR. With the help of this argument, it was clear that the designed EXL ALFR-PB could be operated with the maximum limit of τ_s.

The designed EXL ALFR-PB was suitable for a shear sensitive organism. The shear stress was significantly less compared to conventional equipment. The advantage of this reactor was that gas does not contact immobilized enzymes in the downcomer. Thus, lower shear stress governed less energy input in EXL ALFR-PB and was beneficial for the cultivation of stress-sensitive organisms. Fig. 21 demonstrates a shear stress level as a function of U_G in EXL ALFR-PB.

8. Conclusion

In this study, CFD was successfully used to understand the hydrodynamics of an EXL ALFR equipped with a fixed bed in the downcomer. The hydrodynamic parameters were compared with EXL ALFR. The experimental gas hold-up and liquid circulation velocities were in good agreement with the CFD simulation results. It was observed that the velocity of the circulating liquid was less in EXL ALFR-PB than in EXL ALFR for the same operating condition. The velocity of the circulating liquid increased proportionally with the superficial gas velocity in both reactors. In EXL ALFR-PB, the gas hold-up was more significant than in EXL ALFR for the same operating condition. The bubble residence time was lower due to the lower water circulation velocity in EXL ALFR-PB. The experimental PIV data were collected for five

different superficial gas velocities in both reactors. It was observed that the liquid axial velocity was less in EXL ALFR-PB than in EXL ALFR for the same operating condition. The designed EXL ALFR-PB was more advantageous for cultivating shear-sensitive organisms since the level was significantly lower than that of other gas-liquid contactors. The liquid flow behavior in the downcomer was plug flow in EXL ALFR-PB. The average shear stress in the downcomer was less than 4 Pa for the gas superficial velocity range of 0.02 m/s to 0.1 m/s. The fixed bed of enzymes or catalysts in the downcomer section had comparatively lower shear stress than the conventional reactor. EXL ALFR-PB was found favorable and desirable for applications in stress-sensitive gas-liquid-solid systems.

Conflict of Interest

Authors declare that there is no conflict of interest involved.

Acknowledgement

Authors are thankful to Institute of Chemical Technology, Mumbai, and the Gharda Institute of Technology, Lavel, for support and encouragement.

Funding

This research received no external funding.

Nomenclature

a_{ij}	Interfacial area, m^{-1}
A_d	Cross-sectional area of downcomer, m^2
A_r	Cross-sectional area of a riser, m^2
B_B	The "birth" due to break-up of bubbles, m^{-3} s^{-1}
B_C	The “birth” due to coalescence of bubbles, m^{-3} s^{-1}
C_L	Lift coefficient
C_{vm}	Added/virtual mass coefficients
C_{TD}	Turbulent dispersion coefficient
C_{w1}, C_{w2}	The wall lubrication constants
C_μ, $C_{\varepsilon 1}$, $C_{\varepsilon 2}$,	Constant
$C_{\mu,BI}$	Constant
d_e	Vertical distance between the probes, m
D_B	The "death" due to the break-up of bubbles $m^{-3}s^{-1}$
D_C	The “death” due to coalescence of bubbles m^{-3} s^{-1}
D_P	Diameter of particle, m
d_H	Maximum bubble horizontal dimension of bubble
σ_K, σ_s	Constant
d_e	Vertical distance between the probes, m
d	Diameter of bubble, m
d, di, dj	Diameters (corresponding to m_i and m_j) of the daughter bubbles, m
d_s	Sauter mean bubble diameter, m
fi	Volume fraction of bubbles of group i
f_{BV}	Breakage volume fraction
F_{CB}	Calibration factor
G	Production turbulent kinetic energy, $m^2.s^{-2}$
g	Acceleration due to gravity, $m.s^{-2}$
h_0, h_f	Parameters represent the film thickness when a collision
k	Turbulent kinetic energy, $m^2.s^{-2}$
L	Height of packing, m
n_i	The number density of size group i, m^3
n_j	The number density of size group j, m^3
m_i	Mass of a bubble of group i, kg
m_j	Break-up rate of bubbles of mass, kg
M_I	Total interfacial force acting between two phases, $N.m^{-3}$
$M_{I,L}$	Interfacial forces for liquid,N
$M_{I,G}$	Interfacial forces for gas,N
$M_{D,L}$	Drag force,N
$M_{L,L}$	Lift force,N
$M_{VM,L}$	Virtual mass force,N
$M_{TD,L}$	Turbulent dispersion force,N
$M_{W,L}$	Wall lubricating force,N
ΔP	Dynamic pressure, psi
ΔP_O	Static pressure, psi
r_{ij}	Equivalent radius, m
S_i	Source term due to coalescence and break-up, kg. m^{-3} s^{-1}
S_K	Turbulent kinetic energy dissipation rate added term, $kg{\cdot}m^{-1}{\cdot}s^{-4}$
t_p	Time between the conductivity peaks, s
t	Time, s
t_{ij}	Time required for two bubbles to coalesce having diameter di and dj, s
U_L	liquid circulation velocity, $m.s^{-1}$
V_S	velocity of liquid, m/s
U_G	Superficial gas velocity, $m.s^{-1}$
U_{Ld}	Superficial liquid velocity in the downcomer, $m{\cdot}s^{-1}$
U_{Lr}	Superficial liquid velocity in the riser, $m.s^{-1}$
u	Velocity vector, $m.s^{-1}$
v	Mean velocity, $m.s^{-1}$
$u_i' u_j'$	Fluctuation velocity, $m.s^{-1}$
V_r	Linear velocity of liquid, $m.s^{-1}$
V_T	Terminal velocity, $m.s^{-1}$

Greek Symbols

ϵ_G	Gas hold up
ϵ_L	Liquid hold up

ρ_L	Density of liquid,
ρ_G	Density of gas, $kg.m^{-3}$
μ_L	Viscosity of liquid,Pa.s
μ_G	Viscosity of gas,Pa.s
$\mu_{T.L}$	Viscosity of water,Pa.s
$\mu_{BI,L}$	Viscosity of bubble induced turbulence,Pa.s
$\mu_{eff.L}$	Effective viscosity of liquid,Pa.s
$\mu_{eff.G}$	Effective viscosity of gas,Pa.s
τ_{ij}	Contact time for two bubbles, s
σ	Surface tension, $\mathrm{N.m^{-1}}$
ν_t	Turbulent viscosity, $kg.m^{-1}.s^{-1}$
ν_l	Kinematic viscosity of liquid, $m^2.s^{-1}$
ε_l	Turbulent eddy dissipation rate, $m^2.s^{-3}$
ε	Turbulent energy dissipation rate, $m^2.s^{-3}$
ϵ	Voidage of packing
η	Eddy viscosity , Pa. s
θ_{ij}	The pressure-strain correlation
θ_{ij}^B	Buoyancy collision rate, $m^{-3}\ s^{-1}$
θ_{ij}^S	Laminar shear collision rate $m^{-3}\ s^{-1}$
θ_{ij}^T	Turbulence collision rate $m^{-3}\ s^{-1}$
ξ	Size ratio between an eddy and a particle in the inertial subrange

Subscripts

k	Phase
G	Gas phase
L	Liquid phase
ϵ	Hold-up

Abbreviations

EXL ALFR	External Loop Air Lift Reactor
EL-ALR-PB	External Loop Air Lift Reactor Packed Bed
BCR	Bubble Column Reactor
EXL ALFR-PB	External loop air lift reactor with packed bed
CFD-PBM	Computational Fluid Dynamics Population Balance Model
GLS-FBD	Gas-liquid-solid fluidized beds
FBD	Fluidized beds
ALFR	Airlift Reactor
GLS	Gas Liquid Solid
PIV	Particle Image Velocimetry
MUSIG	Multiple Size Group

References

[1] AL-Mashhadani, M.K.H., Wilkinson, S.J., Zimmerman, W.B. (2015). Airlift bioreactor for biological applications with microbubble mediated transport processes. *Chem Eng Sci., 137,* 243–253.

https://doi.org/10.1016/j.ces.2015.06.032

[2] Karim, K., Hoffmann, R., Klasson, K. T., & Al-Dahhan, M. H. (2005). Anaerobic digestion of animal waste: Effect of mode of mixing. *Water research, 39(15),* 3597-3606.

https://doi.org/10.1016/j.watres.2005.06.019

[3] Karim, K., Klasson, K. T., Hoffmann, R., Drescher, S. R., DePaoli, D. W., & Al-Dahhan, M. H. (2005). Anaerobic digestion of animal waste: Effect of mixing. Bioresource technology, *96(14),* 1607-1612.

https://doi.org/10.1016/j.biortech.2004.12.021

[4] Chisti, M. Y., Halard, B., & Moo-Young, M. (1988). Liquid circulation in airlift reactors. *Chemical Engineering Science, 43(3),* 451-457.

https://doi.org/10.1016/0009-2509(88)87005-2

[5] Mudde, R. F., Van Den Akker, H. E. (2001). 2D and 3D simulations of an internal airlift loop reactor on the basis of a two-fluid model. *Chemical Engineering Science*, *56(21-22),* 6351-6358.

https://doi.org/10.1016/S0009-2509(01)00222-6

[6] Fan, L. S., Muroyama, K., Chern, S. H. (1982). Hydrodynamic characteristics of inverse fluidization in liquid—solid and gas—liquid—solid systems. *The Chemical Engineering Journal, 24(2),* 143-150.

https://doi.org/10.1016/0300-9467(82)80029-4

[7] Delnoij, E., Lammers, F. A., Kuipers, J. A. M., van Swaaij, W. P. M. (1997). Dynamic simulation of dispersed gas-liquid two-phase flow using a discrete bubble model. *Chemical engineering science, 52(9),* 1429-1458.

https://doi.org/10.1016/S0009-2509(96)00515-5

[8] Zhu, J. X., Karamanev, D. G., Bassi, A. S., Zheng, Y. (2000). (Gas-) liquid-solid circulating fluidized beds and their potential applications to bioreactor engineering. *The Canadian Journal of Chemical Engineering, 78(1),* 82-94.

https://doi.org/10.1002/cjce.5450780113

[9] Razzak, S. A., Barghi, S., Zhu, J. X. (2010). Axial hydrodynamic studies in a gas–liquid–solid circulating fluidized bed riser. *Powder*

technology, *199(1)*, 77-86. https://doi.org/10.1016/j.powtec.2009.05.014

[10] Zhou, X., Ma, Y., Liu, M., Zhang, Y. (2020). CFD-PBM simulations on hydrodynamics and gas-liquid mass transfer in a gas-liquid-solid circulating fluidized bed. *Powder Technol., 362,* 57–74. https://doi.org/10.1016/j.powtec.2019.11.060

[11] Fan, L. T., Neogi, D., Yashima, M., Nassar, R. (1990). Stochastic analysis of a three-phase fluidized bed: Fractal approach. *AIChE Journal, 36(10),* 1529-1535.

https://doi.org/10.1002/aic.690361008

[12] Roy, S., Dhotre, M.T., Joshi, J.B. (2006). CFD simulation of flow and axial dispersion in external loop airlift reactor. *Chemical Engineering Research and Design, 84, 677–690*. https://doi.org/10.1205/cherd.05178

[13] Ghadge, R.S., Ekambara, K., Joshi, J.B. (2005). Role of hydrodynamic flow parameters in lipase deactivation in bubble column reactor. *Chem Eng Sci., 60,* 6320–6335.

https://doi.org/ 10.1016/j.ces. 2005.04.045

[14] Freitas, C., Fialová, M., Zahradnik, J., Teixeira, J.A. (2000). Hydrodynamics of a three-phase external-loop airlift bioreactor. *Chem Eng Sci., 55,* 4961–4972.

https://doi.org/10.1016/S0009-2509(00)00130-5

[15] Douek, R.S., Livingston, A.G., Johansson, A.C., Hewitt, G.F. (1994) Hydrodynamics of an external-loop three-phase airlift (TPAL) reactor. *Chem Eng Sci., 49,* 3719–3737. https://doi.org/10.1016/0009-2509(94)00176-6

[16] Freitas, C., Teixeira, J.A. (1998). Hydrodynamic studies in an airlift reactor with an enlarged degassing zone. *Bioprocess Engineering, 18,* 267–279.

https://doi.org/10.1007/ s00449005 0441

[17] Han, S. J., Tan, R. B. H., & Loh, K. C. (2000). Hydrodynamic behaviour in a new gas-liquid-solid inverse fluidization airlift bioreactor. *Food and bioproducts processing, 78(4),* 207-215.

https://doi.org/10.1205/09603080051065313

[18] Lin, J., Han, M., Wang, T., et al. (2004). Experimental study on the local hydrodynamic behavior of a three-phase external-loop airlift reactor. Ind Eng Chem Res., 43, 5432–5437. https://doi.org/10.1021/ie0304614

[19] Siegel, M.H., Robinson, C.W. (1992). Application of airlift gas-liquid-solid reactors in biotechnology. *Chem Eng Sci., 47,* 3215–3229.

https://doi.org/10.1016/0009-2509(92) 85030-F

[20] Liu, M., Zhang, T., Wang, T., et al. (2008). Experimental study and modeling on liquid dispersion in external-loop airlift slurry reactors. *Chemical Engineering Journal , 139,* 523–531. https://doi.org/10.1016/j.cej.2007.08.027

[21] Lele, S.S., Joshi, J.B. (1992). Modelling of air-lift fluidized bed: optimization of mass transfer. *Chemical Engineering J., 49,* 89–105.

https://doi.org/10.1016/0300-9467(92) 80043-A

[22] Verlaan, P., Vos, J. C., Van T Riet, K. (1989). Hydrodynamics of the flow transition from a bubble column to an airlift-loop reactor. *Journal of Chemical Technology & Biotechnology, 45(2),* 109-121.

https://doi.org/10.1002/jctb.280450204

[23] Hamood-Ur-Rehman, M. (2012). Mixing Characteristics of External Loop Airlift Bioreactor using Electrical Resistance Tomography. presented to Ryerson University in partial fulfillment of the requirements for the degree of Master of Applied Science in the program of Chemical Engineering Toronto, Ontario, Canada, 2012.

https://pdfs.semanticscholar.org/2110/90573f15e049caec747e5231ef8cd4fa1b41.pdf

[24] Joshi, J.B. (2001). Computational flow modelling and design of bubble column reactors. *Chem Eng Sci., 56,* 5893–5933.

https://doi.org/10.1016/S0009-2509(01)00273-1

[25] Joshi, J. B., Ranade, V. V., Gharat, S.D. and Lele S.S. (1990). Sparged Loop Reactors. *Canadian Journal of Chemical Engineering, 68,*705–741.

https://doi.org/10.1002/cjce.5450680501

[26] Bendjaballah N., Dhaouadi H., Poncin S., et al. (1999). Hydrodynamics and flow regimes in external loop airlift reactors. *Chem Eng Sci., 54,* 5211–5221.

https://doi.org/10.1016/S0009-2509(99)00242-0

[27] Lu, X., Long, B,, Ding, Y,, Deng, F. (2019). Experimental Study and CFD-PBM Simulation of the Unsteady Gas-Liquid Flow in an Airlift External Loop Reactor. *Flow Turbul Combust., 102,* 1053–1073.

https://doi.org/10.1007/s10494-018-9992-5

[28] Silva, M,K,, d'Ávila, M.A., Mori, M.(2011). CFD modelling of a bubble column with an external loop in the heterogeneous regime. *Canadian Journal of Chemical Engineering, 89,* 671–681.

https://doi.org/10.1002/cjce.20417

[29] Zhang, S., Lv, Z.Y., Muller, D., Wozny, G. (2017). PBM-CFD Investigation of the Gas Holdup and Mass Transfer in a Lab-Scale Internal Loop Airlift Reactor. *IEEE Access, 5,* 2711–2719.

https://doi.org/10.1109/ACCESS.2017.2666542

[30] Law, D., Battaglia, F. (2013). Numerical Simulations for Hydrodynamics of Air-Water External Loop Airlift Reactor Flows with Bubble Break-Up and Coalescence Effects. *J Fluids Eng., 135,* 081302.

https://doi.org/10.1115/1.4024396

[31] Sevugamoorthy, D., & Rangarajan, S. (2023). Comparative analysis of biodegradation and characterization study on algal-assisted wastewater treatment in a bubble column photobioreactor. *Environmental Challenges, 10,* 100659.

https://doi.org/10.1016/j.envc. 2022.100659

[32] Kuś, T., & Madejski, P. (2024). Analysis of the Multiphase Flow With Condensation in the Two-Phase Ejector Condenser Using Computational Fluid Dynamics Modeling. *Journal of Energy Resources Technology, 146(3),* 1-12. https://doi.org/10.1115/1.4064195

[33] Yang, S., Ren, B., Yang, L., Chen, C., Lu, Q., & Wei, Z. (2024). Investigation of the impact of near-wall mesh size on the transition from microscopic wall boiling mechanism to macroscopic multiphase-CFD models. Applied Thermal Engineering, *244,* 122678. https://doi.org/10.1016/j.applthermaleng.2024.122678

[34] Majhool, A. K., Sukkar, K. A., & Alsaffar, M. A. (2023). Combining α-Al_2O_3 packing material and a ZnO nanocatalyst in an ozonized bubble column reactor to increase the phenol degradation from wastewater. *Processes, 11(8),* 2416.

https://doi.org/10.3390/pr11082416

[35] Kulkarni, S. J. (2024). Multifaceted and Diverse Applications of Nanocomposites. In R. Garg & A. Anjum (Eds.), Smart and Sustainable Applications of Nanocomposites (pp. 67-101). IGI Global.

https://doi.org/10.4018/979-8-3693-1094-6.ch003

[36] Kulkarni, S. J. (2023). Combinations of Biotechnology and Nanotechnology in Industrial Wastewater Treatment. In B. Mishra (Ed.), Sustainable Science and Intelligent Technologies for Societal Development (pp. 96-106). IGI Global.

https://doi.org/10.4018/979-8-3693-1186-8.ch006

[37] El Aissaoui El Meliani, M. E. A., Sun, M., Amen, T. W., Choubane, H., Iddou, A., Liu, B., & Terashima, M. (2022). Optimization of an activated sludge process equipped with a diffused aeration system: Investigating the diffuser density sensitivity. *Advances in Environmental Technology, 8(4),* 255-270.

https://doi.org/10.22104/aet.2022.5455.1479

[38] Sharma, M., Mohapatra, T., & Ghosh, P. (2021). Hydrodynamics, mass and heat transfer study for emerging heterogeneous Fenton process in multiphase fluidized-bed reactor system for wastewater treatment—A review. *Chemical Engineering Research and Design, 171,* 48-62.

http://dx.doi.org/10.1016/j.cherd.2021.04.019

[39] Yang, Y. C., Zeng, S. S., Ouyang, Y., Sang, L., Yang, S. Y., Zhang, X. Q, Huang, Y.,Y., Ye.,J.,Xiao, M.T. Zhang, N. (2021). An intensified ozonation system in a tank reactor with foam block stirrer: Synthetic textile wastewater treatment and mass transfer modeling. *Separation and Purification Technology, 257,* 117909. https://doi.org/10.1016/j.seppur.2020.117909

[40] Kandasamy, S., Venkatachalam, S. (2021). Prediction of bed voidage in multi-phase fluidized bed using Air/Newtonian and non-Newtonian liquid systems. *Desalination and Water Treatment, 211,* 92-98.

[41] Oates, A. J. (2021). Coupling Hydrodynamic and Biokinetic Growth Models in Aerated Wastewater Treatment Processes (Doctoral dissertation, University of Leeds). https://etheses.whiterose.ac.uk/29963/

[42] Sampaio, E. F., Rodrigues, C. S., Lima, V. N., & Madeira, L. M. (2021). Industrial wastewater treatment using a bubble photo-Fenton reactor with continuous gas supply. *Environmental Science and Pollution Research, 28(6),* 6437-6449. https://doi.org/10.1007/s11356-020-10741-z

[43] Desireddy, S., & Sabumon, P. C. (2021). Development of aerobic granulation system for simultaneous removal of C, N, and P in sequencing batch airlift reactor. *Journal of Environmental chemical engineering, 9(5),* 106100. https://doi.org/10.1016/j.jece.2021. 106100

[44] Silva, R. M., Fernandes, A. M., Fiume, F., Castro, A. R., Machado, R., & Pereira, M. A. (2021). Sequencing batch airlift reactors (SBAR): a suitable technology for treatment and valorization of mineral oil wastewaters towards lipids production. *Journal of Hazardous Materials, 409,* 124492. https://doi.org/10.1016/j.jhazmat.2020.124492

[45] Praveenkumar, T. R., Alahmadi, T. A., Salmen, S. H., Verma, T. N., Gupta, K. K., Gavurová, B., & Sekar, M. (2024). Impact of sludge density and viscosity on continuous stirred tank reactor performance in wastewater treatment by numerical modelling. *Journal of the Taiwan Institute of Chemical Engineers,* 105368. https://doi.org/10.1016/j.jtice.2024.105368

[46] Sekar, M., Raja, G. G., Salmen, S. H., Chinnathambi, A., Gavurova, B., & Praveenkumar, T. R. (2024). Hydrodynamic cavitation phenomena and flow instabilities in wastewater treatment: A multiphase VOF study with a venturi cavitator. *Journal of the Taiwan Institute of Chemical Engineers*, 105355. https://doi.org/10.1016/j.jtice.2024.105355

[47] Ni, S., Zhao, T., Sun, Z., Wang, W., & Su, K. (2024). CFD simulation for comparative of hydrodynamic effects in biochemical reactors using population balance model with varied inlet gas distribution profiles. *International Journal of Chemical Reactor Engineering*, *(0)*. https://doi.org/10.1515/ijcre-2023-0167

[48] Elaissaoui Elmeliani, M. E. A., Aguedal, H., Iddou, A., Alaoui, C., Benaissa, B., Belhadj, M. E. A., N Guyen, T., Sun, M. & Terashima, M. (2024). Optimizing the Disinfection Inactivation Efficiency in Wastewater Treatment: A Computational Fluid Dynamics Investigation of a Full-Scale Ozonation Contactor. *Chemical Engineering & Technology, 47(1),* 46-55. https://doi.org/10.1002/ceat.202300232

[49] Arshad, M. Y., Ahmad, A. S., Mularski, J., Modzelewska, A., Jackowski, M., Pawlak-Kruczek, H., & Niedzwiecki, L. (2024). Pioneering the Future: A Trailblazing Review of the Fusion of Computational Fluid Dynamics and Machine Learning Revolutionizing Plasma Catalysis and Non-Thermal Plasma Reactor Design. *Catalysts, 14(1),* 40. https://doi.org/10.3390/catal14010040

[50] Le Nepvou De Carfort, J., Pinto, T., & Krühne, U. (2024). An Automatic Method for Generation of CFD-Based 3D Compartment Models: Towards Real-Time Mixing Simulations. *Bioengineering, 11(2),* 169. https://doi.org/10.3390/bioengineering11020169

[51] Wang, Z., Zeng, Y., Pan, Z., Shen, L., Zeng, B., Teng, J., & Lin, H. Improving Dye Biodegradability in Wastewater Using Optimized Water Distribution and Hydrolysis

Acidification. Available at SSRN 4690270. https://dx.doi.org/10.2139/ssrn.4690270

[52] Gao, Y., Saedi, Z., Shi, H., Zeng, B., Zhang, B., & Zhang, X. (2024). Machine Learning-Assisted Optimization of Microbubble-Enhanced Cold Plasma Activation for Water Treatment. *ACS ES&T Water, 4(2),* 735–750. https://doi.org/10.1021/acsestwater.3c00783

[53] Seyed Sharifi, M., Taheriyoun, M., & Qandari, H. (2024). Analyzing the effects of different patterns of diffuser layouts on air distribution and mixing quality in an aeration tank using CFD. *Process Safety and Environmental Protection, 181,* 182-194. https://doi.org/10.1016/j.psep.2023.11.026

[54] Sandoval, M. A., & Domínguez-Jaimes, L. P. (2024). Fluoride removal from drinking water by electrocoagulation process: recent studies, modeling, and simulation through computational fluid dynamics approach. *In Advances in Drinking Water Purification* (pp. 163-179). Elsevier. https://doi.org/10.1016/j.enconman.2023.117832

[55] Teli, S., & Kulkarni, S. (2023). Stirred tank reactor with dual impeller Rushton turbine for application of wastewater treatment-Process optimization and CFD simulation. *Advances in Environmental Technology, 9(3),* 174-193. https://doi.org/10.22104/aet.2023.6207.1710

[56] Zhang, W., Yang, Y., Qian, W., Ma, L., Chen, L., Liu, N., Liu, Y. & Chen, Y. (2023). Numerical research on biomass wastewater treatment using double-partition vessel with off-centered impellers. *International Journal of Agricultural and Biological Engineering, 16(2), 232-240.* http://dx.doi.org/10.25165/j.ijabe.20231602.7637

[57] Sadino-Riquelme, M. C., Donoso-Bravo, A., Zorrilla, F., Valdebenito-Rolack, E., Gómez, D., & Hansen, F. (2023). Computational fluid dynamics (CFD) modeling applied to biological wastewater treatment systems: An overview of strategies for the kinetics integration. *Chemical Engineering Journal, 466,* 143180-14318. https://doi.org/10.1016/j.cej.2023.143180

[58] Hernández-Rodríguez, I. A., López-Ortega, J., González-Blanco, G., & Beristain-Cardoso, R. (2023). Performance of the UASB reactor during wastewater treatment and the effect of the biogas bubbles on its hydrodynamics. Environmental Technology*, 44(16),* 2386-2394. https://doi.org/10.1080/09593330.2022.2028015

[59] Sutudehnezhad, N., Heydarinasab, A., Yegani, R., & Shariati, F. P. (2023). A CFD simulation and experimental study: The impact of aerator design on the bubble flow pattern, foulant removal and scouring capability of flat sheet membrane bioreactor (FSMBR). *Journal of Water Process Engineering, 56,* 104469.

[60] Dottei, A., Holtz, D., & Müller, K. (2023). Numerical investigation of sewage sludge combustion in a fluidized bed reactor: A comparison of 2D and 3D simulations. *Powder Technology, 428,* 118834. https://doi.org/10.1016/j.powtec.2023.118834

[61] Teli, S. M., & Mathpati, C. (2021). Hydrodynamic studies in sectionalised external loop air lift reactors. Indian Chemical Engineer*, 63(1),* 34-49. https://doi.org/10.1080/00194506.2019.1689185

[62] Sivasubramanian, V., & Prasad, B. N. (2009). Effects of superficial gas velocity and fluid property on the hydrodynamic performance of an airlift column with alcohol solution. *International Journal of Engineering, Science and Technology, 1(1),* 245-253. https://doi.org/10.4314/ijest.v1i1.58083

[63] Atenas, M., Clark, M., Lazarova, V. (1999). Holdup and liquid circulation velocity in a rectangular air-lift bioreactor. *Industrial & engineering chemistry research, 38(3),* 944-949. https://doi.org/10.1021/ie980052l

[64] Jiang, X., Yang, N., & Yang, B. (2016). Computational fluid dynamics simulation of hydrodynamics in the riser of an external loop

airlift reactor. *Particuology, 27,* 95-101. https://doi.org/10.1016/j.partic.2015.05.011

[65] Sato, Y., Sadatomi, M., Sekoguchi, K. (1981). Momentum and heat transfer in two-phase bubble flow—I. Theory. *International Journal of Multiphase Flow, 7(2),* 167-177. https://doi.org/10.1016/0301-9322(81)90003-3

[66] Tabib, M. V., Roy, S. A., Joshi, J. B. (2008). CFD simulation of bubble column—an analysis of interphase forces and turbulence models. *Chemical Engineering Journal, 139(3),* 589-614. https://doi.org/10.1016/j.cej.2007.09.015

[67] Chen, Z., Jiang, Z., Zhang, X., & Zhang, J. (2016). Numerical and experimental study on the CO_2 gas–liquid mass transfer in flat-plate airlift photobioreactor with different baffles. *Biochemical engineering journal, 106,* 129-138. https://doi.org/10.1016/j.bej.2015. 11.011

[68] Lu, C., Qi, N., Zhang, K., Jin, J., & Zhang, H. (2009). Experiment and CFD simulation on gas holdup characteristics in an internal loop reactor with external liquid circulation. International *Journal of Chemical Reactor Engineering, 7(1).* https://doi.org/10.2202/1542-6580.1518

[69] Clift, R., Grace, J. R., & Weber, M. E. (1978). Bubbles, drops and particles. Mineola, New., *Reprint Courier coporation*, 2005.

[70] Teli, S. M., & Mathpati, C. S. (2021). Experimental and numerical study of gas-liquid flow in a sectionalized external-loop airlift reactor. *Chinese Journal of Chemical Engineering, 32,* 39-60. https://doi.org/10.1016/j.cjche.2020.10.023

[71] Tomiyama, A., Celata, G. P., Hosokawa, S., & Yoshida, S. (2002). Terminal velocity of single bubbles in surface tension force dominant regime. *International journal of multiphase flow, 28(9),* 1497-1519. https://doi.org/10.1016/S0301-9322(02)00032-0

[72] Bothe, D., Schmidtke, M., & Warnecke, H. J. (2006). VOF-simulation of the lift force for single bubbles in a simple shear flow. *Chemical Engineering & Technology: Industrial Chemistry-Plant Equipment-Process Engineering-Biotechnology, 29(9),* 1048-1053. https://doi.org/10.1002/ceat.200600168

[73] Drew, D. A., Lahey Jr, R. T. (1987). The virtual mass and lift force on a sphere in rotating and straining inviscid flow. *International Journal of Multiphase Flow, 13(1),* 113-121. https://doi.org/10.1016/0301-9322(87)90011-5

[74] Milne-Thomson, L.M. (1968) Theoretical Hydrodynamics, 5th Edition, Dover Publications, New York.

[75] Burns, A. D., Frank, T., Hamill, I., & Shi, J. M. (2004). The Favre averaged drag model for turbulent dispersion in Eulerian multi-phase flows. *In 5th international conference on multiphase flow, 4,* 1-17. Japan: ICMF.

[76] Lopez De Bertodano, M., Lahey, R.T., Jones, O.C. (1994). Development of a k-ε model for bubbly two-phase flow. *Journal of Fluids Engineering, Transactions of the ASME, 116,* 128–134. https://doi.org/10.1115/1.2910220

[77] Antal, S.P., Lahey, R.T., Flaherty, J.E. (1991). Analysis of phase distribution in fully developed laminar bubbly two-phase flow. *International Journal of Multiphase Flow, 17,* 635–652. https://doi.org/10.1016/0301-9322(91)90029-3

[78] Krepper, E., Lucas, D., Prasser, H.M. (2005). On the modelling of bubbly flow in vertical pipes. *Nuclear Engineering and Design, 235,* 597–611. https://doi.org/10.1016/j.nucengdes.2004.09.006

[79] Luo, H. S.H. (1996). Theoretical model for drop and bubble breakup in turbulent dispersions. *AIChE Journal, 42(5),* 1225–33. https://doi.org/10.1002 /aic.690420505

[80] Miller Donald, N. (1974). Scale-up of agitated vessels gas-liquid mass transfer. *AIChE Journal, 20,* 445–453. https://doi.org/10.1002/aic.690200303

[81] Ekambara, K., Joshi J.B. (2008). CFD Simulation of Residence Time Distribution and Mixing in Bubble Column Reactors. *Can J Chem Eng., 81,* 669–676. https://doi.org/10. 1002/cjce.5450810345

[82] Swiderski, K., Narayanan, C., Lakehal, D. (2016). Application of N-phase algebraic slip

model and direct quadrature method of moments to the simulation of air-water flow in vertical risers and bubble column reactor. *Comput Chem Eng, 90,* 151–160. https://doi.org/10.1016/j.compchemeng.2016.04.023

[83] Wang, X., Sun, X. (2009). CFD simulation of phase distribution in adiabatic upward bubbly flows using interfacial area transport equation. *Nucl Technol., 167,* 71–82. https://doi.org/ 10.13 182/N T09-A8852

[84] Cheung, S. C., Yeoh, G. H., Tu, J. Y. (2007). On the modelling of population balance in isothermal vertical bubbly flows—average bubble number density approach. *Chemical Engineering and Processing: Process Intensification, 46(8),* 742-756. https://doi.org/10.1016/j.cep.2006.10.004

[85] Frank, T., Zwart, P.J., Krepper, E., et al .(2008). Validation of CFD models for mono- and polydisperse air-water two-phase flows in pipes. *Nuclear Engineering and Design, 238,* 647–659. https://doi.org/10.1016/j.nucengdes.2007.02.056

[86] Krepper, E., Lucas, D., Frank, T., et al. (2008). The inhomogeneous MUSIG model for the simulation of polydispersed flows. *Nuclear Engineering and Design, 238,*1690–1702. https://doi.org/10.1016/j.nucengdes.2008.01.004

[87] Podila, K., Al Taweel, A.M., Koksal, M., et al (2007) CFD simulation of gas-liquid contacting in tubular reactors. *Chem Eng Sci., 62,* 7151–7162. https://doi.org/10.1016/j.ces .2007.08.081

[88] Huh, B.G. (2006). Mechanistic study for the interfacial area transport phenomena in an air / water flow condition by using fine-size bubble group model. *International Journal of Heat and Mass Transfer, 49,* 4033–4042. https://doi.org/10.1016/j.ijheatmasstransfer.2005.11. 037

[89] Lo, S., Zhang, D. (2009). Modelling of break-up and coalescence in bubbly two-phase flows. *Journal of Computational Multiphase Flows, 1,* 23–38. https://doi.org/10.1260/ 17574820 9787387106

[90] Zuber, N., Findlay, J.A. (1965). Average volumetric concentration in Two-Phase Flow Systems. *J Heat Transfer, 87,* 453–468. https://doi.org/10.1115/1.3689137

[91] Elias, C.B., Joshi, J.B. (1998). Role of hydrodynamic shear on activity and structure of proteins. *Adv Biochem Eng Biotechnol, 59,* 47–71. https://doi.org/10.1007/BFb0102296

How to site this paper:

Teli, Sh. & Kulkarni, S. (2024). CFD with the Population Balance Model for Packed Bed Airlift Reactor with External Loop. Advances in Environmental Technology, 10(3), 237-269. doi: 10.22104/aet.2024.6677.1824